Rivera-Durán, Y.; Muñoz-Cobo, JL.; Cuadros, J.; Berna, C.; Alberto Escrivá (2021). Experimental study of the effects produced by the changes of the liquid and gas superficial velocities and the surface tension on the interfacial waves and the film thickness in annular concurrent upward vertical flows. Experimental Thermal and Fluid Science. 120:1-19. https://doi.org/10.1016/j.expthermflusci.2020.110224

# Experimental study of the effects produced by the changes of the liquid and gas superficial velocities and the surface tension on the interfacial waves and the film thickness in annular concurrent upward vertical flows

Yago Rivera, José-Luis Muñoz-Cobo, José-Luis Cuadros, César Berna, Alberto Escrivá

Universitat Politècnica de València, Instituto de Ingeniería Energética, Building 8E, Camino de Vera s/n, Valencia 46022, Spain

Abstract

## Introduction

In this paper, we have performed an experimental study of the effect of changing the surface tension of the water in vertical annular concurrent two-phase flow (air + liquid) by adding small amounts of 1-butanol to the liquid phase. Adding small amounts of this chemical compound diminishes the surface tension of the water, while the dynamic viscosity remains practically unchanged. A set of experiments have been performed in the interval of surface tension values that ranges from 72. $10^{-3}$ N/m to 45. $10^{-3}$ N/m, and with different values of the superficial velocities of the gas and liquid flows. In this broad range of surface tensions and boundary condition values the following magnitudes which characterize the interface behavior have been measured, average amplitude and frequency of the disturbance waves for each boundary condition and surface tension value. In addition, the mean amplitude of the ripple waves, the mean value of the unperturbed base thickness, and the average film thickness were also measured. A set of correlations have been obtained expressing all these magnitudes in nondimensional form in terms of the Reynolds number of the gas, the Reynolds number of the liquid and the Kapitza number. A brief discussion and comparison with the results of other authors have been also carried out.

Keywords: Interfacial waves, disturbance waves, ripple waves, annular flow

## Introduction

Annular concurrent vertical two-phase flow appears in a big number of nuclear reactor applications as for instance in the vertical channels of Boiling Water Reactors, Advanced Boiling Water Reactors, and in several accidental scenarios of the reactor channels of PWR. In addition, this flow pattern also appears in chemical reactors, and other chemical and energy technologies. When this flow pattern takes place inside a pipe, a liquid film forms close to the pipe walls and moves upward dragged by the shear stress exerted by the gaseous phase. Gas phase moves with much higher velocity than film's velocity and is located in the central part of the pipe, forming a gaseous core with small drops. Generally large waves, denoted as disturbance waves (DW), which are coherent over

large distances appear at the gas-liquid interface. Additionally, incoherent small waves are observed between these large disturbance waves, which popularly are known as ripples waves (RW). The small drops, which appear in annular flow are separated and does not aggregate forming large droplets as in wispy flow.

These large-scale disturbance waves are separated by a thin film liquid layer known as the base film layer, the small scale RW are travelling over this base film layer surface or over the large scale DW. Some authors, as Azzopardi (1997), and Alekseenko et al. (2018), consider the presence of these large DW as a necessary condition for the inception of entrainment. Since they assume that the entrained drops are formed in the peaks or crests of these waves by the shear stress forces exerted by the gas on the top of these waves, which are able to overcome the liquid cohesion forces. Alamu and Azzopardi (2011) showed experimental evidence of the relationship between periodicity/frequency of the DW with respect to the fluctuation (frequency) of the drop concentration in time.

An important issue is the interaction between the DW and the RW, by high speed fluorescence Alekseenko et al. (2014) have shown that RW appear always at the base of the rear front of large DW. In addition, Chu and Dukler (1974) have proved that the RW have a short life in comparison with that of the DW.

Early studies on disturbance waves were performed by Taylor, Hewitt and Lacey (1963), they found that the formation of these waves was related with an observed transition in droplet entrainment which is consistent with the recent findings by Alekseenko et al. (2018). Besides, Taylor et al. (1963) found that the average wave velocity increased rapidly when the gas flow increased but was insensitive to the changes in the liquid flow rate. In addition, they also found that the frequency of these DW was insensitive to the air flow rate but increased with the liquid flow rate. Zhao et al. (2013) found that the DW once are formed remain axially and circumferentially coherent. In addition, small ripples and no coherent waves appeared, which were located between the DW and in some cases mounted on the DW.

In addition, a set of authors have performed previous studies on this subject specially we must mention the works by Belt et al. (2010), and Azzopardi and Whalley (1980) which performed a set of measurements in vertical annular flow, of the film thickness, velocity of the DW, and distribution of these waves.

The main goal of this paper is to perform a set of experiments adding small amounts of 1-butanol to the water. The effect of this addition is to reduce the surface tension of the water while the viscosity remains practically unchanged, this effect is like to rise the water temperature. Proceeding in this way, it is possible to study the effect of the changes of the surface tension on the disturbance waves and ripples wave properties, and to obtain more general correlations for the magnitudes that characterizes these waves.

The organization of the paper is as follows: section 2 describes the vertical annular flow facility (VAFF), the instrumentation used to perform the measurements of the physical magnitudes, and the calibration methods. In section 3, we describe the conductance probe measurements and methods, the test matrix of the experiments, the main magnitudes being measured as height and frequency of the DW, average thickness of the film, properties of the ripple waves and so on. In section 4, we correlate the

nondimensionalized physical magnitudes in terms of pi-monomial, discussing the results. Finally, in section 5, we give the main conclusions of the paper.

## 2. The Vertical annular flow facility (VAFF), instrumentation, data acquisition and calibration methods

### 2.1 Layout, operation, and characteristics of the VAFF facility

In this section, we give a short description of the VAFF facility and its operation. Figure 1 displays the main characteristics of the VAFF facility. This facility includes the following interconnected circuits and components:

i) The air production circuit, which is formed by the following components: i-1) the compressor; i-2) a big air tank, that acts as a reservoir of air to maintain the air flow constant; i-3) a gas filter, that removes any small particle which is being entrained by the gas stream; i-4) a demisting filter to eliminate any small drop or mist contained in the air current; i-5) the flow control valve, that controls that the gas flow is within certain operating limits; i-6) the pressure control valve; i-7) an air flow meter to measure the gas flow entering the test section; i-8) a pressure sensor to measure the pressure near the inlet of the test section.

ii) The water circuit with the following functions: to recover, filter, and store, the water coming from the test section, and then to pump and inject it into the test section through the water injection device (figure 1). This system is formed by the following components and devices: ii-1) the extraction water device, which extracts the water annular film from the test section, this water is removed through a metallic porous material to the water extraction tank, this water is then pumped and after being filtered is send again to the water injection tank; ii-2) The injection water device, which creates the annular flow as shown in figure 1. The water flow between the tank injection system and the test section depends of the pressure difference between both sides of the porous pipe in the injection device.

iii) The test section, that has a height of 5 meters and 44 mm of inner diameter, is made of methacrylate. In the lower part of the test section, this component is connected to the injection device, which creates the annular flow, while its upper part is connected to the extraction device and the demisting cyclone. Therefore, the test section receives an annular flow that develops through the pipe of the test component. Two differential pressure sensors, located in the upper part of the test section, measure the pressure drop of the annular flow at different points to know if the annular flow is fully developed or not (Cuadros et al. 2019). In the upper part of the test section, it is also located the conductance probe that measures the film thickness evolution with time.

The operation of the facility is performed as follows: filtered and demisted air is injected in the lower part of the injection device that creates the annular flow by means of the air production circuit, which contains a compressor whose maximum working pressure and volumetric flow rate are 8 bars and 3750 liters/min respectively. The flow rate of the injected air ranges from 2250 to 3500 liters/min. At the same time, the injection water device injects the water in the test section, at a lower flow rate ranging from 4 to 10

liters/min. The water film flow created by this injection device is pushed up by the shear stress acting on the gas-water interface produced by the gas flow moving upward at much higher velocity than that of the water annulus close to the walls. This water-gas flow develops through the test section and disturbance and ripple waves are produced at the interface, which are registered by the conductance probe located in the upper part of the test section. The characteristics of these waves depend on the boundary conditions, mainly gas and liquid superficial velocities ($j_l$ and $j_g$) and liquid surface tension ($\sigma$). This last effect is analyzed adding small quantities of 1-butanol to the water that modifies the surface tension producing small variations on the viscosity.

The gas flow, when its velocity is high enough, can drag small drops from the crest of the disturbance waves that then move with the gas stream. Some of these drops, due to the turbulence motion, can interact with the water film flow, and others move toward the exit of the test section and enter a centrifugal demisting cyclone, where are separated from the gas stream. The demisted gas stream is then vented to atmosphere. New fresh air is injected into the test section after compression, demisting and filtering, and a new air cycle starts again.

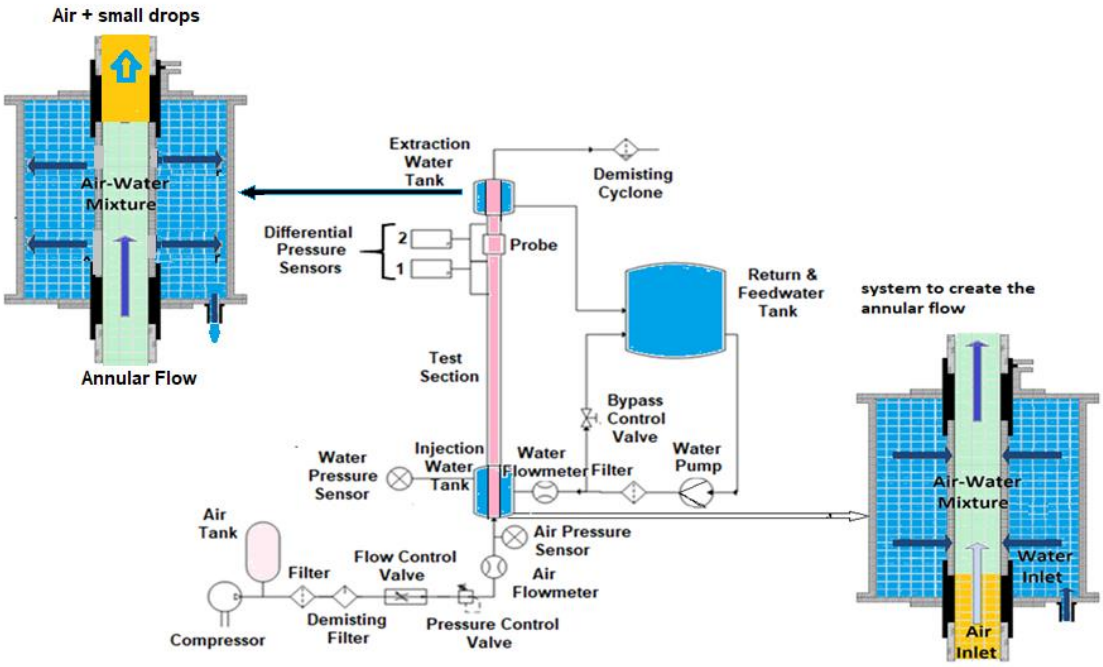


Figure 1: Layout of the vertical annular flow facility (VAFF) with a description of the water injection and extraction systems, which create the annular flow and remove the water film respectively.

## 2.2 Facility instrumentation, electronics and data acquisition

### 2.2.1 Main facility instrumentation

The VAFF facility is equipped with different sensors and probes to check all the state variables and the boundary conditions. All the measurements are performed when the annular flow is completely developed at the measuring point for each experimental

condition. To check this issue, two differential pressure sensors, denoted as 1 and 2, are located in the upper part of the test section, if both sensors measure the same pressure drop this means that the flow is fully developed. The equipment used to perform these measurements is formed by two SMC PSE 550 low differential pressure transducers. These sensors have a rated pressure range from 0 to 2 kPa, with an accuracy ±1.0% at full scale (F.S.) or smaller, a linearity error equal or less than ±0.5% F.S., and a repeatability error of 0.3% F.S. or less.

Because, according to Darcy formula (Cuadros et al. 2019), the volumetric flow rate depends on the pressure difference between the inner and outer sides of the porous sintered material, then the local pressure measurements are made at two different points, one in the water injection tank and the other one near the inner side of the porous sintered pipe, see figure 1 for more details. These local measurements are performed with Burkert 8314 relative pressure transducers (difference in pressure between the inner part of the facility and the surrounding atmosphere). These sensors have a pressure range measurement between 0 and 1 bar, with a sum of linearity, hysteresis and repeatability errors less than ±0.3% F.S. and error adjustment accuracy zero point and full scale less than ±0.3%.

The temperature of the water was measured during the experiment and an average value was computed for each particular run with given boundary conditions and 1-butanol concentration which determines a surface tension value ($j_l$, $j_g$ and $\sigma$). Temperature measurements were performed with Type T thermocouples (copper-constantan), which are suitable in the range -200 to 350 ºC. Their error, for measurements above 0ºC, is the biggest one of the following two values 1.0ºC and 0.75% of the measured temperature in Celsius degrees.

The water volumetric flow rate measurements were performed with a Krohne Optiflux 4300 C Series electromagnetic flowmeter (EMF). This EMF was located in the pipe that supplies the water to the injection device. Its volumetric flow rate measurement interval ranges from 0 to 20 l/min and has an accuracy better than ±0.3% of span.

The measurements of the high-speed gas volumetric flow rate were performed with a SMC PF2A706H magnetic flowmeter. Its volumetric flow rate measurement range covers from 300 to 6000 l/min, the flowmeter has a linearity accuracy of ±1.5 % of full scale (F.S.) or less and a repeatability of ±1.5 % F.S. or less.

2.2.2 Conductance probe characteristics

The estimation of the characteristics of the interfacial waves and the film thickness is performed using a conductance probe. This type of probe, which is displayed in figure 2-b, allows to measure and record the fast-moving wavy film behaviour produced at the gas-liquid interface. This probe consists in three conducting electrodes flush mounted to the wall and aligned with the tube in the direction of the gas and film flows. The first electrode is the transmitter electrode, which emits a signal generated by a signal-generator, the second one is connected to the ground and the third one is the receiver electrode, which collects the current that the water film conduces. The amount of current conducted from the emitter to the receiver depends on the film thickness existing between both electrodes. The three electrodes are inserted into the conductance probe port that is

made of polypropylene. In addition, the three sensor electrodes are made of stainless steel and are inserted in the port vertically to the port walls as displayed in figure 2-b, the space between the electrodes is 1.5 mm, and have a diameter of 2 mm. The transmitter electrode is excited, with a 300 kHz sinusoidal signal and 4 Volts peak to peak. The diameter of the port is the same one that the diameter of the pipe and its length is 170 mm. Small slots have been created at both sides of the port to connect it to the test pipe without connection discontinuities.

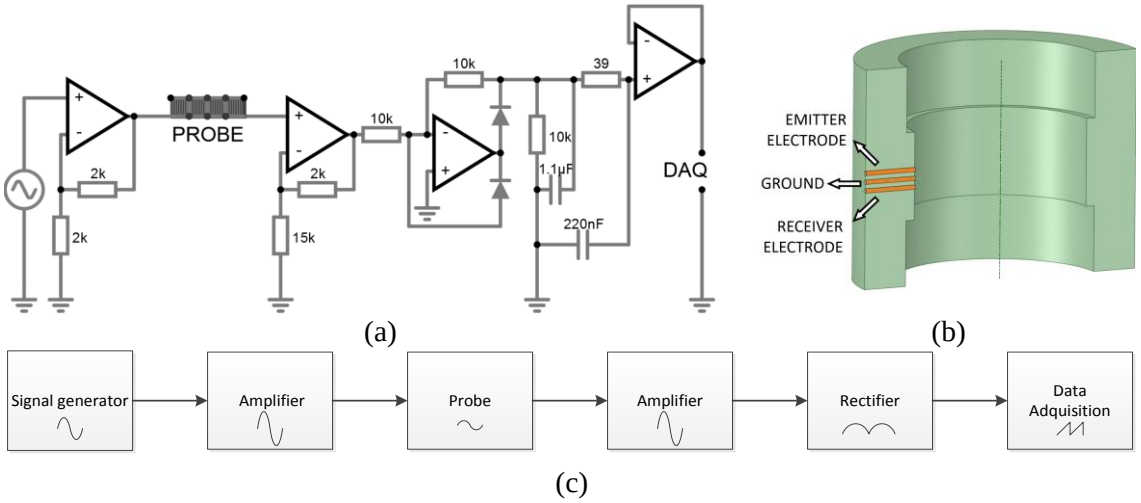


Figure 2 a) Electronic circuit built for the conductance probe, b) 3D view of the probe with the arrangement of the 3 electrodes, c) flow diagram of the performance of the electronic circuit.

The total amount of current collected by the receiver at any time instant is proportional to the liquid film thickness existing at that time between both electrodes, i.e., the transmitter and the receiver. Also, it is important to notice that the resistance and capacitance between the transmitter and receiver electrodes depends also on the signal frequency. Because of the resistance and the capacitance fall to asymptotic values as the frequency increases, for this reason the frequency of the signal was set to 300 kHz, which is beyond the frequency saturation point. The dependence of the signal voltage with the film thickness has been analyzed by several authors for different types of conductance probes (Coney 2001, Koskie et al. 1989, Kyu Byung Lee et al. 2016). All of them have found that the signal in volts increases with the film thickness, being necessary a calibration that depends of the fluid conductivity and the characteristics of the conductance probe. Consequently, the electric signal collected by the receiver changes when an interfacial wave crosses the sensor region for a conducting liquid as water, and this change allows the determination of the liquid film thickness variations with time.

### 2.2.3 Electronics and data acquisition system

The electronic used for the conductance probe is displayed at figure 2-a, the functions performed are: first the sinusoidal signal produced by the generator is amplified before sending it to the excitation electrode or transmitter (Rivera et al. 2019). Next, the receiver electrode captures the signal, which has been transmitted through the liquid layer. This last signal is amplified again and transformed into a DC current by a rectifier incorporated

to the electronics device. Finally, the data acquisition system acquires this DC signal, whose value is related to the liquid film thickness existing between both electrodes. As consequence, the variations with time in the value of this DC signal will indicate the passage of the interfacial waves present in the liquid film. This electronic circuit is made of 4 high frequency amplifiers, several precision resistances (0.1% tolerance), capacitances and diodes 1N4148. All the components used are high precision ones, with low tolerance.

During the test runs all the instrumentation devices, located in the positions given at figure 1 and described in the previous sections, are monitoring in real time. In order to acquire all the major experimental conditions, the collected data include air and water volumetric flow rates, temperatures and pressures, in addition to the recording of the experimental data along the test section, i.e., conductance probe signal in volts and pressure test-section values. The data acquisition system has been programmed in LabView. This system distinguishes between two types of measurements: The conductance probe measurements, which suffer fast variation with time and need high sample rates in order to capture the shape of the wave peaks, and the rest of measurements as temperature, pressure and flow rates, which need much smaller sample rates. The acquisition system for the conductance probe records $10^5$ samples per second (S/s) (National Instruments PCI 6255 with 80 analogic channels and a maximum rate of 1.25 MS/s). For the rest of experimental data, which suffer smaller variations with time, the acquisition system records 120 samples per minute from each sensor of the facility (National Instruments cDAQ-9174 chassis compact-DAQ with a module NI 9207 of 16 analogic channels and a maximum rate of 500 S/s).

### 2.3 Calibration of the conductance probe

To obtain better accuracy (Rivera et al. 2019) than in previous measurements (Cuadros et al. 2019) a new calibration device, displayed at figure 3, was designed and built with higher precision components than the previous one. The goal of the calibration is to relate the voltage signal with the water film thickness. For the measurement performed adding 1-butanol to the water, the sensor calibration must be repeated, because water conductivity changes with 1-butanol concentration and therefore the electric signal is different for each 1-butanol concentration when the rest of conditions are the same. Proceeding is this way, it is possible to relate the information contained in the recorded signals (V) with the amplitude of the waves (mm) and film thicknesses (mm) produced at the fluid interface.

The calibration process was carried out with the calibration device, displayed at figure 3. This device consists of three major components: one optical precision table; a precision positioning system mounted on this table with an error of 0.002 mm; and several cylinders with known diameters and made with a dielectric material. By setting the dielectric cylinder at the desired position, in the inner part of the conductance probe port, by means of the precision positioning system, we can know the fluid thickness between the dielectric and the probe electrodes inserted in the polypropylene port and connected to the electronics displayed at figure 3. Then, measuring the voltage in the receiver electrode of the probe for each film thickness, we can find by a fitting process the existing relationship between the signal voltage and the fluid thickness.

A total number of 33 calibration measurements were made with the calibration device for each one of the three 1-isobutanol concentrations values, which are denoted by their surface tensions at 25 ºC, $68.5 \cdot 10^{-3}$ N/m, $55 \cdot 10^{-3}$ N/m and $45 \cdot 10^{-3}$ N/m. As shown in Figure 4, all the calibration measurements saturated beyond a given thickness, i.e., the signal in volts attained a saturation value.

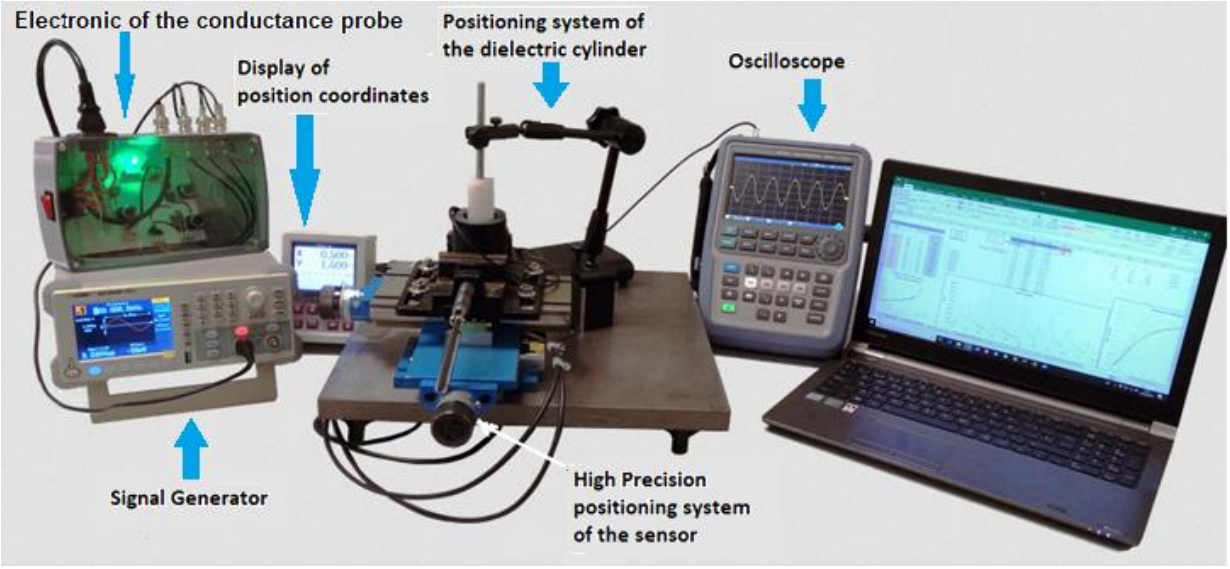


Figure 3. Arrangement of elements of the high precision calibration device for the conductance probe.

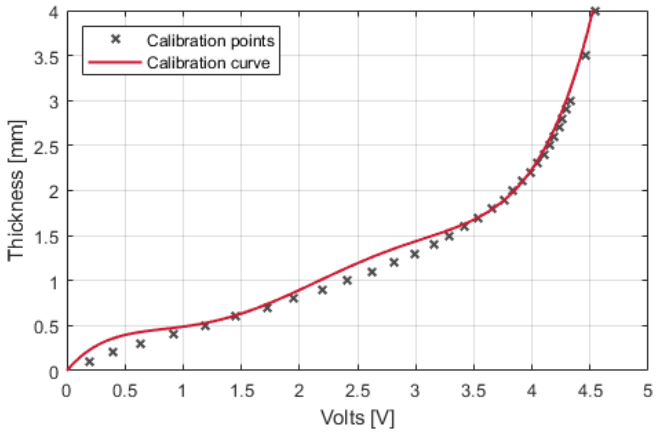


Figure 4. Calibration curve obtained with 33 calibration points and a fitting polynomial of fifth degree for $\sigma = 68.5 \cdot 10^{-3}\ N/m$.

However, as the experimental data for the boundary conditions used in this paper showed that the signal amplitudes (Volts) were smaller than 0.8 Volts for all the cases with 1-butanol, then the film thickness and the height of the disturbance waves were always smaller than 1.5 mm for all the experimental condition used. Therefore, the boundary conditions of these experiments were far away to produce disturbance waves and film thicknesses which attained the saturation conditions. So, we reduced the number of calibration points including only those below 1.5 mm, which are inside the area marked in grey at figure 5, the number of points inside this shadowed area was 16. Another

advantage of performing a fitting in this reduced region is that the curve slope has smaller changes in this region, and therefore the fitting can be performed with a polynomial of smaller degree and better determination coefficient ($R^2$), practically one for the fits performed.

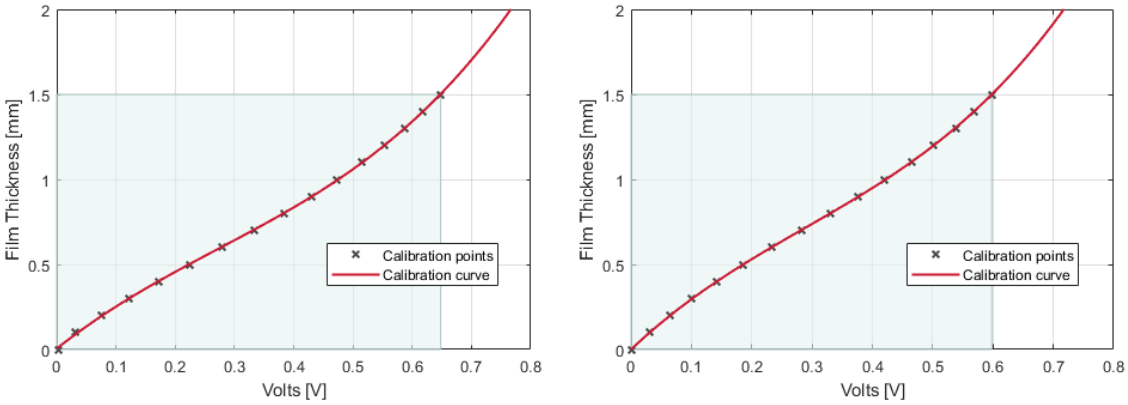


Figure 5. Calibration curve obtained using a third degree polynomial fit for two of the experiments performed adding (a) 1-butanol to the water to reach $55 \cdot 10^{-3}$ N/m and (b) $45 \cdot 10^{-3}$ N/m.The crosses denote the experimental points and the shadowed area the region were all the experimental values of this paper are found and the calibration points selected.

The calibration curve used to fit the 1-butanol calibration experiments was a third degree polynomial given by eq. (1), with coefficients denoted by the symbols $x_0$ to $x_3$, while for pure water the fitting curve was also given by eq. (1):

$$\delta(mm) = x_0 + x_1 V + x_2 V^2 + x_3 V^3 \quad (1)$$

The coefficient of determination of the polynomials fits of the calibration curves for all the 1-butanol cases inside the shadowed area was $R^2 = 0.999$.

The expression used to obtain the fitting error $\varepsilon_{fit,cal}$of equation (1), with N=16 experimental data points, for the 1-butanol cases, and m degrees of freedom (m=4), can be found in chapter 7 of Bevington and Robinson book (2003) and is given by:

$$\varepsilon_{fit,cal} = \sqrt{\frac{1}{N-m}\sum_{j=1}^{N}\left(\delta_{exp,j} - \sum_{i=0}^{3} x_i V_j^i\right)^2} \quad (2)$$

Because of the experimental points display a smooth behavior in the interest region (shadowed area) with small changes of slope as shown in figure 4. Then, a fit was performed using only the calibration point located inside the area of interest and a third degree polynomial, in this way the fitting error was notably reduced in comparison to the result that was obtained using a fifth degree polynomial degree mainly in the region from 0 to 5 Volt as displayed in figure 5. For instance, the fitting error was reduced from 0.282 mm to 0.0059 mm for the case of 1-butanol with surface tension 68.5 $10^{-3}$ N/m. The

coefficient obtained for the calibration curves for each one of the 1-butanol concentrations are displayed in table 1. These curves also display the root mean square error (RMSE), and the fitting error calculated with equation (2).

Table 1. Coefficients of the third-degree polynomial fits obtained for the calibration curves of the different 1-butanol concentrations and the pure water. The last two columns display the coefficient of determination $R^2$ and the root mean square (RMSE) fitting error.

| $\sigma\ (N/m)$ | $x_3$ | $x_2$ | $x_1$ | $x_0$ | $R^2$ | RMSE | $\varepsilon_{fit,cal}$ (mm) |
|---|---|---|---|---|---|---|---|
| 72. $10^{-3}$ | 1.605 | -2.227 | 2.413 | -0.0095 | 0.9992 | 0.0135 | 0.0191 |
| 68.5 $10^{-3}$ | 3.793 | -2.915 | 2.659 | 0.002 | 0.9999 | 0.0051 | 0.0059 |
| 55. $10^{-3}$ | 4.123 | -3.372 | 2.765 | 0.005 | 0.9999 | 0.0049 | 0.0057 |
| 45. $10^{-3}$ | 5.230 | -4.538 | 3.351 | 0.000 | 0.9999 | 0.0026 | 0.0030 |

## 3. Conductance probe measurements: boundary conditions, filtering results and errors.

3.1 Test matrix and boundary conditions

The test matrix consisted of four data series; three performed adding 1-butanol to the water plus one additional with only water. Each one of the 1-butanol data series was performed with a constant concentration of 1-butanol. As the surface tension of the mixture diminishes when the concentration of 1-butanol increases, then we denote the different runs by their respective surface tensions. That is $72 \times 10^{-3}$N/m for the water at 25 ºC, and 68.5 $10^{-3}$ N/m, 55.0 $10^{-3}$ N/m and 45.0 $10^{-3}$ N/m for the different mixtures of water-1-butanol with the concentrations of 1-butanol in increasing order.

For each solution of 1-butanol in water, we performed forty-nine experimental runs, which were obtained by combining seven liquid and seven gas superficial velocities respectively, denoted by $j_l\left(\frac{m}{s}\right)$ and $j_g\left(\frac{m}{s}\right)$. The experimental runs can be also represented by their respective volumetric flow rates, denoted by $Q_l\left(\frac{litters}{minute}\right)$ and $Q_g\left(\frac{litters}{minute}\right)$. The seven liquid flow rates covered the interval from $Q_l = 4$ to 10 l/min, with increments of $\Delta Q_l = 1\left(\frac{litter}{minute}\right)$, or from $j_l = 0.044\, m/s$ to 0.11 m/s with increments $\Delta j_l = 0.011\, m/s$. The seven volumetric air flow rates covered from $Q_g =$ 2000 l/m to 3500 l/m, with increments of $\Delta Q_g = 250\ l/m$ from run to run, or from $j_g =$ 21.9 $m/s$ to 38.4 m/s, with increments $\Delta j_g = 2.75\frac{m}{s}$.

The main goal of changing the water surface tension is to study the effect produced by this change on the interfacial wave's behavior. The interest of this issue is because diminishing the water surface tension value is quite similar to the effect produced by a temperature increment, which also reduces the surface tension. During all the experimental measurements the pressure in the upper part of the facility was kept at

atmospheric conditions, and the water and air temperatures were kept approximately constant at about 30 and 25 ºC respectively.

During each experimental test run, we followed the same procedure used by Cuadros et al. (2019), which consisted in the following four steps:

i) Adjustment of the air and liquid volumetric flow rates to the desired boundary values.

ii) Check that the steady state conditions have been attained for the main variables (air and liquid volumetric flow rates, pressures and differential pressures at the monitored points, and liquid and gas temperatures).

iii) Check that the two-phase annular flow is developed at the measuring point of the conductance probe. This condition is attained when the two differential pressure sensors, located in the upper part of the test section at different positions, provide on average the same value. If the flow is not developed for the set of stablished boundary conditions, this experimental run is discarded. This is the reason to discard all the runs with $Q_l \leq 3\ l/m$, see the paper by Cuadros et al (2019) for more details.

iv) Once the steady state conditions are attained, the facility operator starts the collection and recording of all the data for sixty seconds. The signal from the conductance probe is sampled at a frequency of $10^5$ Samples/s, for sixty seconds that yields a total number of $6.10^6$ samples for each one of the 49 experimental runs performed for each 1-butanol concentration. The signal coming from the other sensors are sampled at a slower rate of 2 Samples/s, which yield 120 samples for each monitored magnitude during the measuring time.

Table 2 display all the boundary conditions used for the 49 experimental runs of one of the four data series, notice that these boundary conditions are repeated for the other three remaining data series.

Table 2. Boundary conditions of the experiments performed in the VAFF facility for each 1-butanol concentration.

| Boundary conditions used for the 49 data series with $\sigma = 45.10^{-3}\ N/m$ | | | | | | |
|---|---|---|---|---|---|---|
| $j_g\ (m/s) \times j_l (m/s)$ | | | | | | |
| 21.92 x 0.044 | 24.66 x 0.044 | 27.40 x 0.044 | 30.14 x 0.044 | 32.88 x 0.044 | 35.62 x 0.044 | 38.36 x 0.044 |
| 21.92 x 0.055 | 24.66 x 0.055 | 27.40 x 0.055 | 30.14 x 0.055 | 32.88 x 0.055 | 35.62 x 0.055 | 38.36 x 0.055 |
| 21.92 x 0.066 | 24.66 x 0.066 | 27.40 x 0.066 | 30.14 x 0.066 | 32.88 x 0.066 | 35.62 x 0.066 | 38.36 x 0.066 |
| 21.92 x 0.077 | 24.66 x 0.077 | 27.40 x 0.077 | 30.14 x 0.077 | 32.88 x 0.077 | 35.62 x 0.077 | 38.36 x 0.077 |
| 21.92 x 0.088 | 24.66 x 0.088 | 27.40 x 0.088 | 30.14 x 0.088 | 32.88 x 0.088 | 35.62 x 0.088 | 38.36 x 0.088 |
| 21.92 x 0.099 | 24.66 x 0.099 | 27.40 x 0.099 | 30.14 x 0.099 | 32.88 x 0.099 | 35.62 x 0.099 | 38.36 x 0.099 |
| 21.92 x 0.110 | 24.66 x 0.110 | 27.40 x 0.110 | 30.14 x 0.110 | 32.88 x 0.110 | 35.62 x 0.110 | 38.36 x 0.110 |

The physical magnitudes, which were monitored, sampled and stored during each experimental data run were: air and water volumetric flow rates, i.e., $Q_g$and $Q_l$, liquid and gas temperatures ($T_l$ and $T_g$ respectively), and pressures at the entrance to the test section and in the water injection tank to the test section. In addition to the conductance probe voltage signal collected by the receiver electrode and amplified by the electronic system displayed in figures 2-a and 2-c.

3.2 Conductance probe measurements and errors

From the probe signal in Volts (raw data), we applied first the corresponding calibration functions to each one of the signals for the different experimental data runs of each data series with different 1-butanol concentrations. In this way, the signals in volts versus time, were converted in signals in mm versus time. These signals give the evolution of the film thickness of the water plus 1-butanol mixture versus time. Figure 6 displays the evolution of the film thickness versus time for the raw signals for the run case of 2250 litters/min x 7 litters/min ($Q_g \times Q_l$), and different values of the surface tension in N/m.

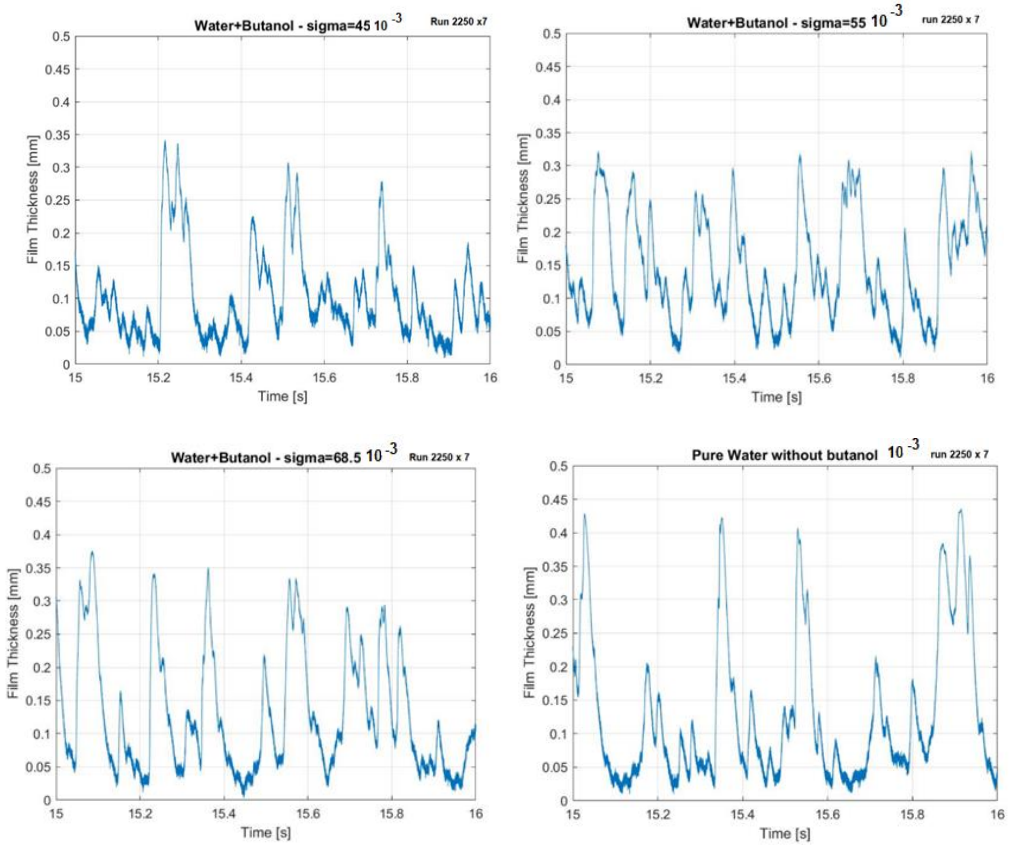


Figure 6. Film thickness versus time for $Q_g \times Q_l$ runs 2250 x 7 for different 1-butanol concentrations, with $\sigma$ values of 45 $10^{-3}$ N/m, 55 $10^{-3}$ N/m, 68.5 $10^{-3}$ N/m, and 72. $10^{-3}$ N/m, before applying the Savitzky-Golay moving average filter.

The next step was to apply a Savitzky-Golay moving average filter to the raw data. The reason to use this kind of filter is because this type of filters preserve the width and height of the peaks, while standard moving average filters tends to broad the peaks and to reduce their heights as commented by Press et al. (1992). In addition, the Savitzky-Golay filter (1962) produces very little distortion in the signal in comparison to the standard moving average filters (Guiñon et al. 2007). The application of this filter is performed choosing several points or frame length (m), to obtain each component of the filtered signal and a set of coefficients ($c_i$), which are known as the convolution coefficients. In this filter, if we denote by $\{y_k\}$ the sampled signal. Then the Savitzky-Golay filtered signal $\{y_{SG}(j)\}$ is given by the expression:

$$y_{SG}(j) = \sum_{i=-n_p}^{n_p} c_i \; y_{j+i} \tag{3}$$

Where $n_p = (m-1)/2$ and the convolution coefficients $c_i$ are obtained by a least square polynomial fit to all the points inside each moving average window. If the degree of the fitting polynomial is p, this means that the polynomials have the form $a_0 + a_1 i + \cdots + a_p i^p$. The fit is performed selecting the set of coefficients $c_i$ by a least-square fitting to the m signal points contained in the window, which gives the following result:

$$c_i = \sum_{l=0}^{p} \{(A^T A)^{-1}\}_{0l} \, i^l \tag{4}$$

Being $A^T$ the transpose of A, that is the matrix with elements given by:

$$A_{il} = i^l \tag{5}$$

The elements of $A^T A$ are easy to obtain and are given by:

$$(A^T A)_{il} = \sum_{k=-n_p}^{n_p} A_{ik}^T \, A_{kl} = \sum_{k=-n_p}^{n_p} A_{ki} \, A_{kl} = \sum_{k=-n_p}^{n_p} k^{i+j} \tag{6}$$

The calculation of the inverse $(A^T A)^{-1}$ is simple because, according to equation (4), we only need the elements of the first row.

The application of this filter has been performed choosing a polynomial of order p=8 and several window points or frame length m=101. The results obtained by application of the Savitzky-Golay filter to the signals of case $Q_g \times Q_l = 2250 \times 7$, for different 1 butanol concentrations are displayed in figure 7. We observe that the height of the peaks and their widths remain practically unchanged after application of this filter.

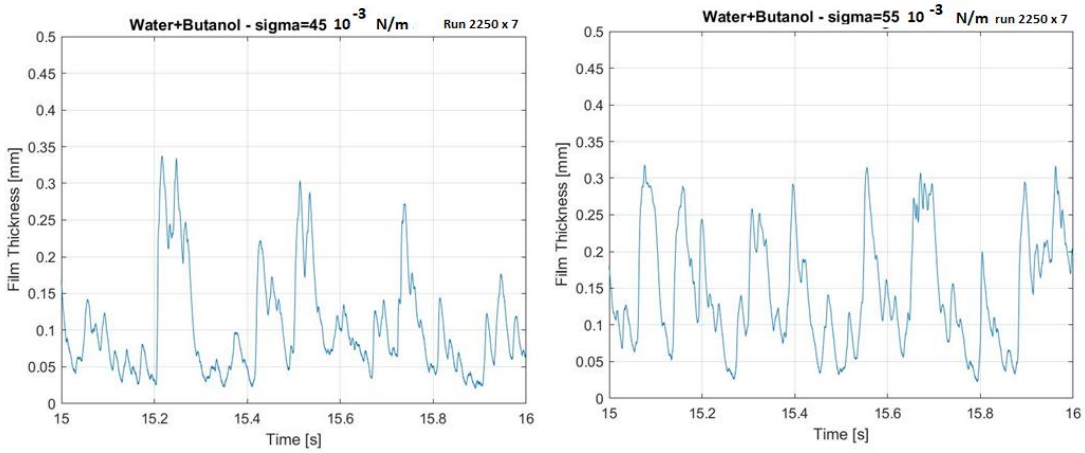

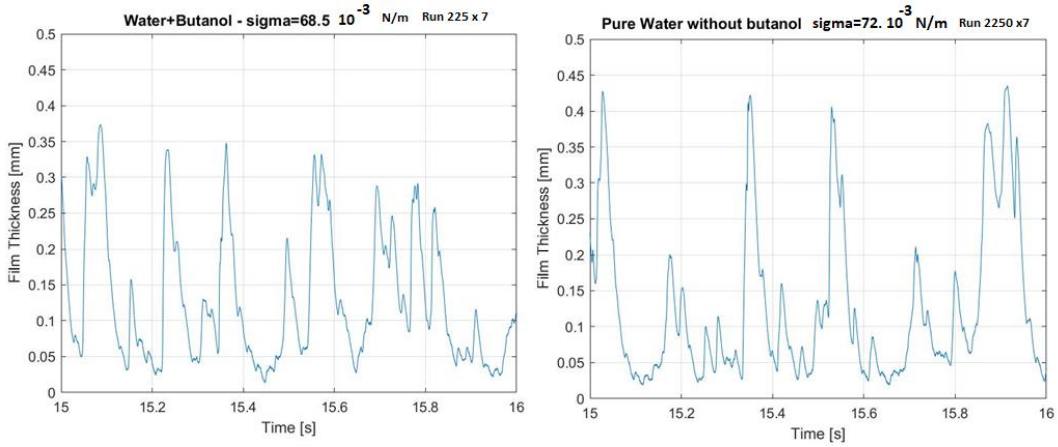


Figure 7. Film thickness versus time for $Q_g \times Q_l$ runs 2250 x 7 for different 1-butanol concentrations, with $\sigma$ values of 45 $10^{-3}$ N/m, 55 $10^{-3}$ N/m, 68.5 $10^{-3}$ N/m, and 72. $10^{-3}$ N/m, after application of the Savitzky-Golay moving average filter.

It is observed from figures 6 and 7 that the height of the disturbance waves increases when the surface tension increases, i.e. when the 1-butanol concentration diminishes. This is equivalent to say that the height of the disturbance waves diminishes when we increase the temperature of the fluid. We remind here that the surface tension of the water at saturation temperature and atmospheric pressure is 58.92 $10^{-3}\ N/m$, so the selected range of interfacial tensions covers a good range of values that can be found in practical applications.

The total error has been obtained from the following expression:

$$\varepsilon_\delta = \sqrt{\left(\frac{\partial f(V)}{\partial V}\right)^2 \varepsilon_V^2 + \varepsilon_{fit,cal}^2 + \varepsilon_{pos}^2 + \varepsilon_{acc}^2}\ , \tag{7}$$

Where $f(V)$ is the polynomial calibration function given by equation (1), $\varepsilon_V$is the error of the equipment used to measure the voltage, $\varepsilon_{fit,cal}$ is the fitting error given by expression (2), $\varepsilon_{pos}$ is the position error during the calibration process, and finally $\varepsilon_{acc}$ is the accidental error, that is calculated by the expression:

$$\varepsilon_{acc}(\delta) = t_{1-\alpha/2}\frac{S(\delta)}{\sqrt{n}}, \tag{8}$$

Where $\mathrm{t}_{1-\alpha/2}(df)$ is the t-Student of $1-\frac{\alpha}{2}$ quantile for $df = n-1$ degrees of freedom, being n the number of measurements performed, and S the variance. This quantile depends on the confidence level and on the degrees of freedom, having a value of 2.26 for the usual 95% confidence level ($\alpha = 0.05$) and with 9 degrees of freedom, i.e., when the measurements are repeated ten times. The estimated accidental errors and the relative errors in % for the various magnitudes measured in this work are displayed at table (3).

Table 3. Accidental errors obtained from the repeatability analysis for the main physical magnitudes that characterize the interphase.

| | $\varepsilon_{acc}(\delta_m)$ (μm) | $\varepsilon_{acc}(\delta_{bun})$ (μm) | $\varepsilon_{acc}(A_{DW})$ (μm) | $\varepsilon_{acc}(\nu_{DW})$ (Hz) |
|---|---|---|---|---|
| $\varepsilon_{acc}$ | 29.3 | 5.12 | 53.4 | 0.92 |

| $\pm\varepsilon_{rel,acc}$, % | ±6.2 | ±1.76 | ±7.9 | ±4.5 |
|---|---|---|---|---|

The estimated total errors for the average thickness, unperturbed base thickness and amplitude of the DW have been computed from equation (7), on account of the calibration curve for each surface tension value and are displayed in table 4.

Table 4. Total errors for the main magnitudes obtained for the different surface tension values

| $\sigma$ (N/m) | $\varepsilon_{tot}(\delta_m)$ (μm) | $\varepsilon_{tot}(\delta_{bun})$ (μm) | $\varepsilon_{tot}(A_{DW})$ (μm) |
|---|---|---|---|
| $72.\ 10^{-3}$ | 35 | 20 | 57 |
| $68.5\ 10^{-3}$ | 30 | 8 | 54 |
| $55.\ 10^{-3}$ | 29.9 | 8 | 54 |
| $45.\ 10^{-3}$ | 29.5 | 6 | 53 |

3.3 Measurement of the magnitudes that characterize the interfacial waves and the film

The magnitudes that have been estimated in the experiments for the different boundary conditions and surface tensions are: the average amplitude $A_{DW}$ of the disturbance waves, the average thickness $\delta_{b+rw}$ of the base film plus the ripples waves, the mean film thickness $\bar{\delta}_m$, the average thickness $\bar{\delta}_{DW}$ of the disturbance waves, the average thickness $\bar{\delta}_{ripples}$ of the ripple waves, the mean amplitude $A_{ripples}$ of the ripple waves, and the mean frequency $\nu_{DW}$ of the disturbance waves. A schematic view of the interfacial waves and the previously mentioned magnitudes is displayed in figure 8.

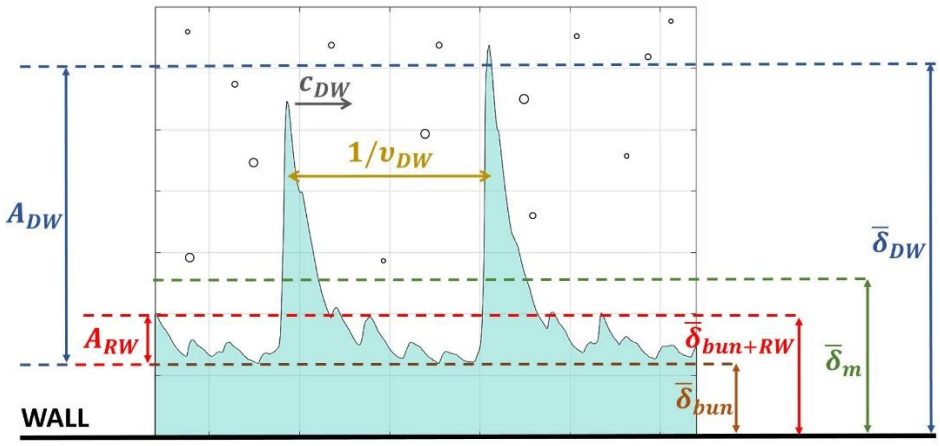


Figure 8. Schematic view of the different magnitudes that characterize the interfacial waves.

3.3.1 Liquid film thickness measurements

Four variables related with the liquid film thickness have been estimated, these are the mean film thickness $\bar{\delta}_m$, the unperturbed-base plus RW film thickness $\bar{\delta}_{bun+rw}$, the unperturbed film thickness $\bar{\delta}_{bun}$, and the average thickness of the DW $\bar{\delta}_{DW}$. The average film thickness is the distance from the pipe wall to the mean height of the film, this include computing the average value of the film thickness in all the film regions, i.e. regions with disturbance waves, region with ripple waves and finally regions without any wave. The $\bar{\delta}_{bun+rw}$ is the average film thickness in the inter-space between disturbance waves, including the ripple waves. Finally, the unperturbed film thickness is the average film distance from the pipe wall to the base of all the waves $\bar{\delta}_{bun}$. Based on these definitions, we can define the average amplitudes of the disturbance waves, $A_{DW}$, and the ripples waves, $A_{RW}$, as follows:

$$A_{DW} = \bar{\delta}_{DW} - \bar{\delta}_{bun} \quad (9)$$

$$A_{RW} = \bar{\delta}_{bun+rw} - \bar{\delta}_{bun} \quad (10)$$

Table 5 displays $A_{RW}$ in mm in the inter-space between disturbance waves. It is observed that $A_{RW}$ increases with the liquid superficial velocity $j_l$ for all the cases and surface tension values. Also, $A_{RW}$ diminishes when the gas volumetric flow rate $Q_g$ increases. In addition, figure 9 displays the RW amplitude $A_{RW}$ versus $j_l$ for the case with $Q_g = 2500\ litters/min$. This amplitude increases with a small slope with $j_l$. Furthermore, this amplitude shows a small tendency to increase with the increments in the surface tension.

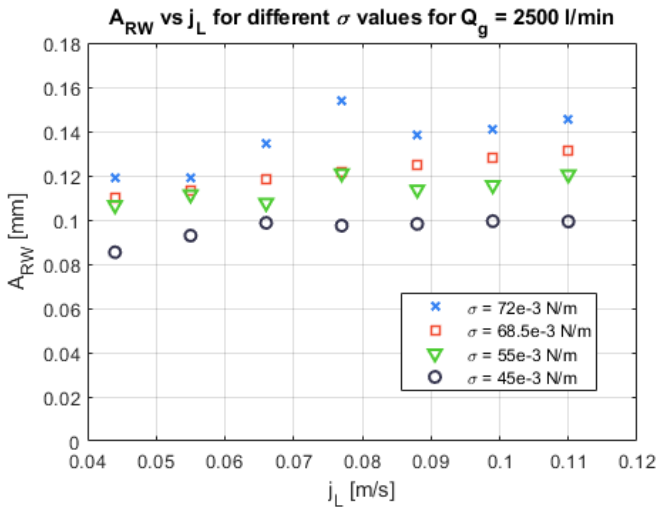


Figure 9. Experimental average amplitude $A_{RW}$ versus $Q_l$ for $Q_g = 2500\ l/m$, and different values of the surface tension series 72 ($\sigma = 72\ 10^{-3} N/m$), series 68 ($\sigma =$ 68.5 $10^{-3}$N/m),series 55 ($\sigma = 55.10^{-3} N/m$), series 45 ($\sigma = 45.10^{-3} N/m$).

Table 5. Average amplitude of the ripple waves $A_{RW}$, for different values of the gas and liquid volumetric flow rates and surface tensions.

| | $A_{RW}\ (mm)$ | | | |
|---|---|---|---|---|
| $Q_g \times Q_l$ | $72.10^{-3}$ | $68.5\ 10^{-3}$ | $55.10^{-3}$ | $45.\ 10^{-3}$ |
| 2500x4 | 0.119 | 0.111 | 0.108 | 0.086 |
| 2500x5 | 0.120 | 0.113 | 0.113 | 0.093 |

| | | | | |
|---|---|---|---|---|
| 2500x6 | 0.135 | 0.119 | 0.109 | 0.099 |
| 2500x7 | 0.154 | 0.121 | 0.122 | 0.098 |
| 2500x8 | 0.139 | 0.125 | 0.115 | 0.098 |
| 2500x9 | 0.141 | 0.128 | 0.118 | 0.099 |
| 2500x10 | 0.146 | 0.132 | 0.122 | 0.099 |
| $Q_g \times Q_l$ | $72.10^{-3}$ | $68.5\ 10^{-3}$ | $55.10^{-3}$ | 45. x $10^{-3}$ |
| 3000x4 | 0.090 | 0.068 | 0.057 | 0.067 |
| 3000x5 | 0.105 | 0.072 | 0.068 | 0.076 |
| 3000x6 | 0.120 | 0.077 | 0.074 | 0.082 |
| 3000x7 | 0.126 | 0.082 | 0.077 | 0.085 |
| 3000x8 | 0.120 | 0.084 | 0.083 | 0.089 |
| 3000x9 | 0.127 | 0.090 | 0.086 | 0.089 |
| 3000x10 | 0.139 | 0.092 | 0.091 | 0.089 |
| $Q_g \times Q_l$ | $72\ 10^{-3}$ | $68.5\ 10^{-3}$ | $55.10^{-3}$ | 45 x $10^{-3}$ |
| 3500x4 | 0.086 | 0.053 | 0.046 | 0.058 |
| 3500x5 | 0.096 | 0.058 | 0.054 | 0.064 |
| 3500x6 | 0.105 | 0.066 | 0.061 | 0.074 |
| 3500x7 | 0.117 | 0.071 | 0.070 | 0.084 |
| 3500x8 | 0.102 | 0.074 | 0.077 | 0.085 |
| 3500x9 | 0.116 | 0.083 | 0.079 | 0.085 |
| 3500x10 | 0.121 | 0.092 | 0.085 | 0.093 |

Concerning the measurements of the unperturbed film thickness, which gives the average film thickness obtained after removing all types of waves and that it is denoted by $\bar{\delta}_{bun}$, it is observed that this base film thickness decreases clearly when increasing the gas flow $Q_{gas}$ for all the surface tension values, as displayed in table 6. However, this parameter is not affected by the surface tension. In addition, there is a small tendency to increase $\bar{\delta}_{bun}$ when the liquid volumetric flow $Q_l$ rises. The value of the unperturbed film thickness is computed by dividing each sensor signal with 60 seconds of recording time, which contains $6.10^6$ data points in 100 sub-intervals of 0.6 s containing $6.10^4$ data points per sub-interval. Each subinterval contains several DW and many RW, then at each subinterval the minimum value of the film thickness is computed and finally the average unperturbed film thickness is defined as the mean of all the minimum values obtained in all the subintervals.

Table 6. Average value of the unperturbed base film thickness $\bar{\delta}_{bun}$ for different gas and liquid volumetric flow rates and surface tensions.

| | $\bar{\delta}_{bun}$(mm) | | | |
|---|---|---|---|---|
| $Q_g \times Q_l$ | $72\ 10^{-3}$ | $68.5\ 10^{-3}$ | $55.10^{-3}$ | 45 x $10^{-3}$ |
| 2500x4 | 0.031 | 0.031 | 0.035 | 0.028 |
| 2500x5 | 0.034 | 0.035 | 0.038 | 0.031 |
| 2500x6 | 0.037 | 0.035 | 0.041 | 0.031 |
| 2500x7 | 0.041 | 0.037 | 0.043 | 0.033 |
| 2500x8 | 0.034 | 0.041 | 0.044 | 0.036 |
| 2500x9 | 0.034 | 0.041 | 0.046 | 0.037 |
| 2500x10 | 0.034 | 0.043 | 0.048 | 0.038 |
| $Q_g \times Q_l$ | $72\ 10^{-3}$ | $68.5\ 10^{-3}$ | $55.10^{-3}$ | 45 x $10^{-3}$ |
| 3000x4 | 0.027 | 0.021 | 0.020 | 0.024 |

| | | | | |
|---|---|---|---|---|
| 3000x5 | 0.030 | 0.022 | 0.021 | 0.026 |
| 3000x6 | 0.033 | 0.023 | 0.024 | 0.028 |
| 3000x7 | 0.035 | 0.024 | 0.025 | 0.029 |
| 3000x8 | 0.028 | 0.024 | 0.026 | 0.030 |
| 3000x9 | 0.030 | 0.026 | 0.028 | 0.032 |
| 3000x10 | 0.032 | 0.027 | 0.030 | 0.032 |
| $Q_g \times Q_l$ | 72 $10^{-3}$ | 68.5 $10^{-3}$ | 55. $10^{-3}$ | 45 x $10^{-3}$ |
| 3500x4 | 0.028 | 0.021 | 0.019 | 0.023 |
| 3500x5 | 0.030 | 0.022 | 0.022 | 0.025 |
| 3500x6 | 0.031 | 0.023 | 0.024 | 0.027 |
| 3500x7 | 0.034 | 0.025 | 0.025 | 0.029 |
| 3500x8 | 0.024 | 0.026 | 0.027 | 0.031 |
| 3500x9 | 0.025 | 0.027 | 0.028 | 0.032 |
| 3500x10 | 0.027 | 0.030 | 0.029 | 0.034 |

Another important magnitude that have been measured is the average mean thickness, which is defined as the distance from the pipe wall to the film surface, obviously this include to consider the surface points located in the DW, in the RW and in regions without waves. This magnitude is denoted as $\bar{\delta}_m$. Table 7 displays the mean film thickness for different values of $Q_{gas}$, $Q_l$ and the liquid surface tensions, $\sigma$. From this table, it is concluded that the average film thickness diminishes with the increases of the gas superficial velocity and also with the increments of the surface tension. Also, there is an increase produced in $\bar{\delta}_m$ by the increments of the liquid superficial velocity, $j_l$.

Table 7. Average film thickness $\bar{\delta}_m(mm)$ for different gas and liquid superficial velocities in units of m/s and different surface tensions $\sigma$ in N/m.

| | | $\bar{\delta}_m(mm)$ | | | |
|---|---|---|---|---|---|
| $j_g \times j_l$ | $Q_g \times Q_l$ | 72.$10^{-3}$ | 68.5 $10^{-3}$ | 55. $10^{-3}$ | 45. $10^{-3}$ |
| 21.92x0.044 | 2000x4 | 0.318 | 0.282 | 0.241 | 0.192 |
| 21.92x0.055 | 2000x5 | 0.383 | 0.292 | 0.243 | 0.199 |
| 21.92x0.066 | 2000x6 | 0.395 | 0.302 | 0,242 | 0.215 |
| 21.92x0.077 | 2000x7 | 0.425 | 0.318 | 0.243 | 0.201 |
| 21.92x0.088 | 2000x8 | 0.451 | 0.314 | 0.240 | 0.203 |
| 21.92x0.099 | 2000x9 | 0.471 | 0.311 | 0.235 | 0.193 |
| 21.92x0.110 | 2000x10 | 0.500 | 0.307 | 0.230 | 0.189 |
| 27.4x0.044 | 2500x4 | 0.194 | 0.197 | 0.179 | 0.137 |
| 27.4x0.055 | 2500x5 | 0.219 | 0.211 | 0.200 | 0.155 |
| 27.4x0.066 | 2500x6 | 0.252 | 0.229 | 0.219 | 0.169 |
| 27.4x0.077 | 2500x7 | 0.275 | 0.244 | 0.234 | 0.178 |
| 27.4x0.088 | 2500x8 | 0.299 | 0.255 | 0.235 | 0.186 |
| 27.4x0.099 | 2500x9 | 0.304 | 0.267 | 0.244 | 0.188 |
| 27.4x0.110 | 2500x10 | 0.330 | 0.283 | 0.249 | 0.190 |
| 32.88x0.044 | 3000x4 | 0.136 | 0.113 | 0.089 | 0.103 |
| 32.88x0.055 | 3000x5 | 0.167 | 0.121 | 0.111 | 0.120 |
| 32.88x0.066 | 3000x6 | 0.190 | 0.132 | 0.125 | 0.134 |
| 32.88x0.077 | 3000x7 | 0.218 | 0.145 | 0.134 | 0.146 |
| 32.88x0.088 | 3000x8 | 0.226 | 0.153 | 0.146 | 0.155 |
| 32.88x0.099 | 3000x9 | 0.249 | 0.162 | 0.157 | 0.163 |

| | | | | | |
|---|---|---|---|---|---|
| 32.88x0.110 | 3000x10 | 0.276 | 0.172 | 0.169 | 0.165 |
| 38.36x0.044 | 3500x4 | 0.112 | 0.091 | 0.077 | 0.091 |
| 38.36x0.055 | 3500x5 | 0.136 | 0.103 | 0.096 | 0.104 |
| 38.36x0.066 | 3500x6 | 0.150 | 0.114 | 0.107 | 0.122 |
| 38.36x0.077 | 3500x7 | 0,174 | 0.126 | 0.122 | 0.137 |
| 38.36x0.088 | 3500x8 | 0.177 | 0.137 | 0.134 | 0.146 |
| 38.36x0.099 | 3500x9 | 0.201 | 0.149 | 0.141 | 0.155 |
| 38.36x0.110 | 3500x10 | 0.221 | 0.170 | 0.152 | 0.166 |

In general, for a given fixed value of $j_g$ or $Q_g$, the mean film thickness $\bar{\delta}_m$increases with the increments of $Q_l$ and the surface tension $\sigma$, as displayed in figure 10-b, for the case of $Q_g = 2500\ lit/min$. However, these increments in $\bar{\delta}_m$ seems to attain a saturation value above 8 lit/min, for the cases with lower surface tensions. The same behavior is observed for the case with $Q_g = 2250\ lit/min$ as displayed in figure 10-a.

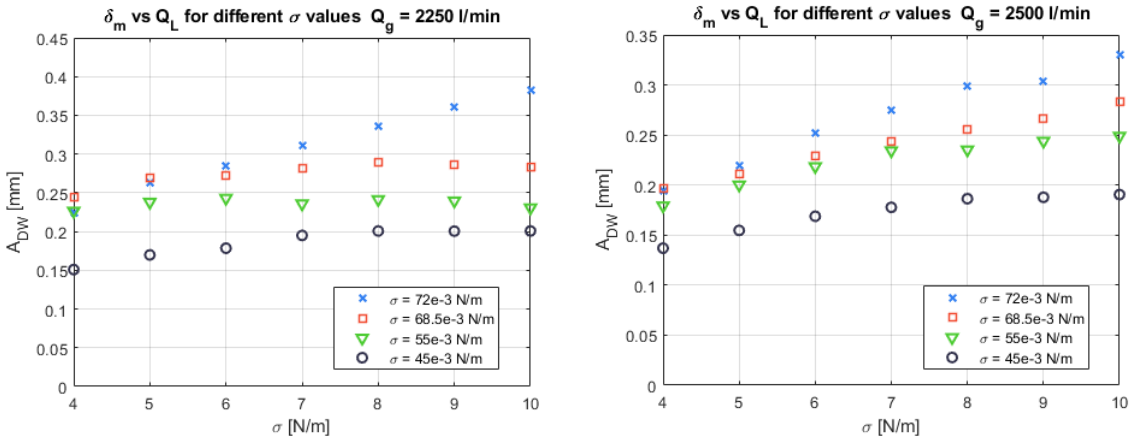


(a) (b)

Figure 10. Mean film thickness $\bar{\delta}_m$versus the volumetric liquid flow rate $Q_l$, for fixed, $Q_g = 2250\ l/m$ (10-a) and $Q_g = 2500\ l/m$ (10-b) and different values of the surface tension series 1 ($\sigma = 72\ 10^{-3} N/m$), series 2 ($\sigma = 68.5\ 10^{-3}$N/m),series 3 ($\sigma = 55.10^{-3} N/m$), series 4 ($\sigma = 45.10^{-3} N/m$).

3.2 Measurements of the disturbance wave amplitudes and frequencies

The amplitude $A_{DW}$ and frequency $\nu_{DW}$ of the disturbance waves were measured for different values of the superficial velocities of the gas and the liquid, and also for different values of the surface tension covering a broad range of values in these magnitudes. To obtain the amplitude of the disturbance waves, we have followed an iterative multi-criteria. The procedure's major aim is to count only the disturbance waves, eliminating from the counting the ripples waves and also to consider as a single peak those in which a crest with multiple close peaks are shown. The first of these criteria is performed choosing a threshold value, as in the papers by De Jong and Gabriel (2003), and Rodriguez (2004), so all the peaks which are below this cut value are eliminated in a first round from the peak counting procedure. As observed in figure 10 (a) all the peaks below 0.2 mm have been removed from the DW counting.

The second criterion concerns the needs to eliminate the multiple small peaks, which appear in the crest of some disturbance waves as observed in figure 10 (a) for the fifth DW, that contains two peaks. This second criterion, which was also considered by Cuadros et al. (2019) and denoted as closeness criterion, is applied as follows, first it is stablished a minimum distance $d_{min,DW}$ between successive DW peaks, so that when the distance between two successive DW peaks is smaller than this value, then it is considered that we have only one DW. For instance, as shown in figure 11-a, we have considered that this minimum distance is $3.10^{-2}s$. Then, because the distance between the two peaks located in the crest of the fifth DW of figure 11-a is smaller than $3.10^{-2}s$ then the MATLAB program consider them as one peak.

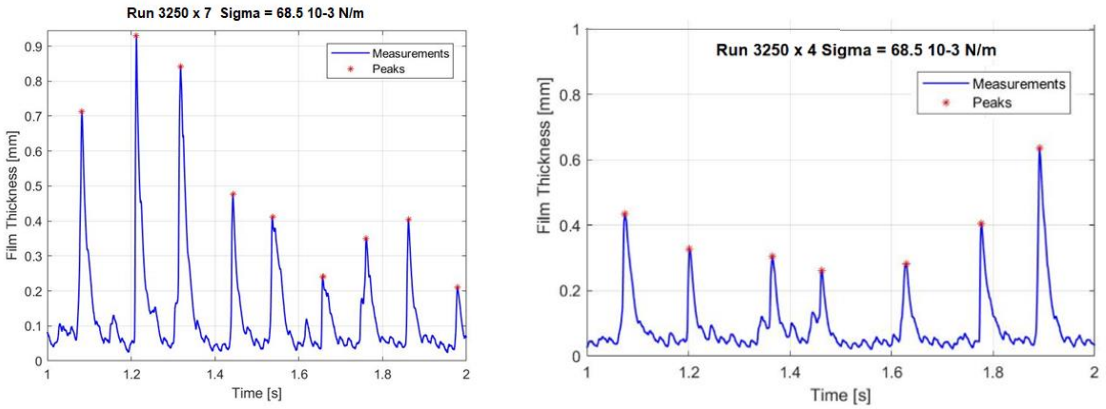


(a) (b)

Figure 11. (a) Identification of the disturbance waves peaks, denoted in the figure by an asterisk (*), by the iterative multi-criteria implemented in a Matlab program for run 3250 x 7 with $\sigma = 68.5\ 10^{-3}N/m$. (b) Identification of DW peaks for run 3250 x 4 with $\sigma = 68.5\ 10^{-3}N/m$.

There is a third criterion to eliminate the ripple waves formed on the disturbance waves and those RW reached by the DW. This criterion, called prominence criterion, is based on a prominence cut value defined as a relative value of the DW amplitude, which serve as threshold criterion. Then, if the relative height of these secondary peaks is smaller than this relative amplitude threshold value, these secondary peaks are considered to be also produced by ripples waves mounting on some part of a DW. These peaks are more frequently formed in the rear part of the disturbance waves, where the slope of the wave is smaller than in the front part, as displayed at figures12-a and 12-b.

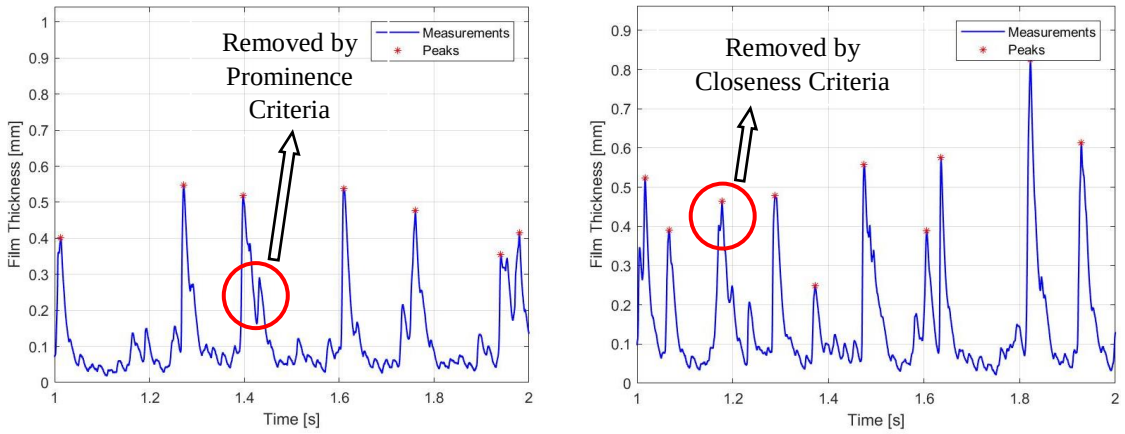

Figure 12. Identification of the disturbance waves peaks, denoted in the figure by an asterisk (*), by the iterative multicriteria implemented in a Matlab program for (a) run 2750 x 5 with $\sigma = 68.5\ 10^{-3} N/m$. (b) Identification of DW peaks for run 2750 x 6 with $\sigma = 68.5\ 10^{-3} N/m$.

After the implementation of this identification multi-criteria of the DW, which removes the waves of small amplitude (RW) and also those RW that are mounted on a DW, we display in table 8, the values of the DW amplitudes, $A_{DW}$, for different gas and liquid volumetric flow rates and surface tensions. This table shows that, in general, when the gas volumetric flow rate increases then the amplitude of the DW decreases. This decrement in the DW amplitude is produced because increases the interfacial shear stress exerted by the gas on the liquid-gas interface, shear stress which tend to diminish the amplitude of the DW and to drag small drops from the crest of these waves. Another clearly observed effect is that $A_{DW}$ diminishes when the surface tension diminishes; this effect is clearly observed for all the cases of the table 8. This means that when the temperature increases and, consequently, the surface tension diminishes, then the DW amplitude will be smaller for the same conditions of the other variables. Concerning the liquid volumetric flow rate, it is observed that the amplitude of the disturbance waves increases for pure water when the liquid flow rate increases. While for the rest of cases, with smaller surface tensions, the effect of the liquid flow rates on the amplitude of the disturbance waves does not show a clear tendency, except for very high gas volumetric flow rates with $Q_g = 3500\ litters/min$.

Table 8. Amplitude of the disturbance waves in mm for different values of $Q_g$ and $Q_l$ in litters/min and different surface tensions in N/m

| | | $A_{DW}(mm)$ | | |
|---|---|---|---|---|
| $Q_g \times Q_l$ | $\sigma$ =72x10$^{-3}$ | 68.5x10$^{-3}$ | 55x10$^{-3}$ | 45x10$^{-3}$ |
| 2500x4 | 0.7502 | 0.6504 | 0.4987 | 0.4384 |
| 2500x5 | 0.7687 | 0.6461 | 0.5070 | 0.4537 |
| 2500x6 | 0.8200 | 0.6499 | 0.4991 | 0.4459 |
| 2500x7 | 0.8642 | 0.6137 | 0.4874 | 0.4287 |
| 2500x8 | 0.8770 | 0.6202 | 0.4708 | 0.4143 |
| 2500x9 | 0.8649 | 0.6073 | 0.4658 | 0.3906 |
| 2500x10 | 0.9180 | 0.6085 | 0.4447 | 0.3777 |
| $Q_g \times Q_l$ | 72x10$^{-3}$ | 68.5x10$^{-3}$ | 55x10$^{-3}$ | 45x10$^{-3}$ |
| 3000x4 | 0.5922 | 0.4887 | 0.3936 | 0.3985 |
| 3000x5 | 0.6588 | 0.4799 | 0.4249 | 0.4083 |
| 3000x6 | 0.7035 | 0.4695 | 0.4245 | 0.4054 |
| 3000x7 | 0.7433 | 0.4733 | 0.4250 | 0.3857 |
| 3000x8 | 0.7817 | 0.4668 | 0.4155 | 0.3755 |
| 3000x9 | 0.7911 | 0.4633 | 0.4084 | 0.3633 |
| 3000x10 | 0.8379 | 0.4682 | 0.4033 | 0.3556 |
| $Q_g \times Q_l$ | 72x10$^{-3}$ | 68.5x10$^{-3}$ | 55x10$^{-3}$ | 45x10$^{-3}$ |
| 3500x4 | 0.5158 | 0.3710 | 0.3470 | 0.3723 |
| 3500x5 | 0.5628 | 0.3948 | 0.3851 | 0.3817 |
| 3500x6 | 0.6114 | 0.4150 | 0.3946 | 0.3945 |
| 3500x7 | 0.6271 | 0.4359 | 0.4143 | 0.3972 |
| 3500x8 | 0.6613 | 0.4449 | 0.4253 | 0.3795 |
| 3500x9 | 0.7032 | 0.4649 | 0.3877 | 0.3621 |

| | | | | |
|---|---|---|---|---|
| 3500x10 | 0.7419 | 0.4930 | 0.4036 | 0.3616 |

The figure 13 displays the variation of the amplitude $A_{DW}$ of the disturbance waves in mm with the surface tension in Newtons/m for a fixed value of the gas superficial velocity equal to $j_g = 21.92\, m/s$. It is observed that the amplitude increases when the surface tension increases for the three values of $j_l$ represented in this figure, i.e., 0.055 m/s (blue points), 0.077 m/s (orange points) and 0.099 m/s (grey points). It is noticed that the influence of liquid superficial velocity on the DW amplitude is small compared with the influence of the surface tension.

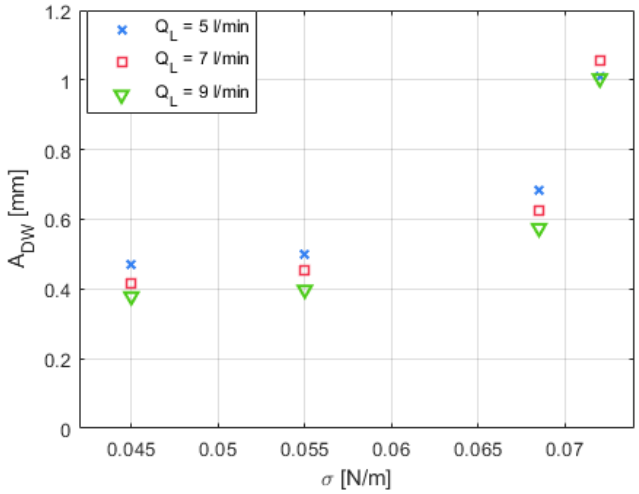


Figure 13. Average amplitude $A_{DW}(mm)$of the disturbance waves versus the surface tension (N/m) for $j_g = 21.92\, m/s$ , and $j_l$ values of 0.055 m/s ($Q_l = 5\frac{l}{min}, data\ 5$), 0.077 m/s ($Q_l = 7\frac{l}{min}, data\ 7$)and 0.099 m/s ($Q_l = 9\frac{l}{min}$, data 9).

The last issue to be analyzed in this section is the frequency of the disturbance waves. The average value of the DW frequency was computed counting the number of DW peaks and dividing by the measuring time interval in seconds. In this way, we have obtained the average frequency of the DW in Hz for each boundary condition. Table 9 shows the frequency of the disturbance waves in Hz for different values of $j_g$ and $j_l$ in m/s and different surface tensions $\sigma$ in N/m. It is observed that the mean frequency $\nu_{DW}$ increases with the liquid superficial velocity $j_l$ for any fixed $j_g$ value, and any fixed surface tension $\sigma$ value. Also figure 14 confirms this result, where it is clearly observed that the frequency increases with the liquid flow rate $Q_l$, for all the surface tension values, when $Q_g$ remains fixed at 3000 l/min ($j_g = 27.4\, m/s$).

Table 9. Frequency $\nu_{DW}$ of the disturbance waves in Hz for different values of $j_g$ and $j_l$ in m/s and different surface tensions in N/m

| | | $\nu_{DW}(Hz)$ | | | |
|---|---|---|---|---|---|
| $j_g \times j_l$ | $Q_g \times Q_l$ | 72 $10^{-3}$ | 68.5 $10^{-3}$ | 55 x$10^{-3}$ | 45 x $10^{-3}$ |
| 21.92x0.044 | 2500x 4 | 7.53 | 7.75 | 7.77 | 5.82 |
| 21.92x0.055 | 2500x 5 | 8.42 | 8.32 | 8.23 | 6.60 |

| | | | | | |
|---|---|---|---|---|---|
| 21.92x0.066 | 2500x 6 | 9.22 | 8.83 | 8.73 | 7.13 |
| 21.92x0.077 | 2500x 7 | 9.30 | 9.98 | 9.67 | 7.42 |
| 21.92x0.088 | 2500x 8 | 9.92 | 9.92 | 9.62 | 7.62 |
| 21.92x0.099 | 2500x 9 | 10.32 | 10.20 | 9.22 | 7.60 |
| 21.92x0.110 | 2500x10 | 10.48 | 10.88 | 9.37 | 7.47 |
| $j_g \times j_l$ | $Q_g \times Q_l$ | 72 $10^{-3}$ | 68.5 $10^{-3}$ | 55 $x10^{-3}$ | 45 x $10^{-3}$ |
| 27.4x0.044 | 3000x4 | 6.95 | 6.92 | 5.45 | 5.73 |
| 27.4x0.055 | 3000x5 | 8.03 | 7.52 | 6.65 | 6,57 |
| 27.4x0.066 | 3000x6 | 8.83 | 8.02 | 7.48 | 7.33 |
| 27.4x0.077 | 3000x7 | 9.55 | 8.85 | 7.98 | 8.35 |
| 27.4x0.088 | 3000x8 | 9.70 | 9.48 | 8.53 | 8.53 |
| 27.4x0.099 | 3000x9 | 10.45 | 9.67 | 9.00 | 9.18 |
| 27.4x0.110 | 3000x10 | 10.67 | 10.17 | 9.72 | 9.13 |
| $j_g \times j_l$ | $Q_g \times Q_l$ | 72 $10^{-3}$ | 68.5 $10^{-3}$ | 55 $x10^{-3}$ | 45 x $10^{-3}$ |
| 32.88x0.044 | 3500x4 | 5.48 | 8.15 | 6.05 | 6.20 |
| 32.88x0.055 | 3500x5 | 7.02 | 8.93 | 7.37 | 7.02 |
| 32.88x0.066 | 3500x6 | 7.50 | 9.28 | 7.87 | 8.00 |
| 32.88x0.077 | 3500x7 | 8.70 | 9.75 | 8.47 | 8.75 |
| 32.88x0.088 | 3500x8 | 9.48 | 10.38 | 9.00 | 9.60 |
| 32.88x0.099 | 3500x9 | 9.98 | 10.38 | 10.07 | 10.60 |
| 32.88x0.110 | 3500x10 | 10.47 | 11.28 | 10.72 | 10.75 |

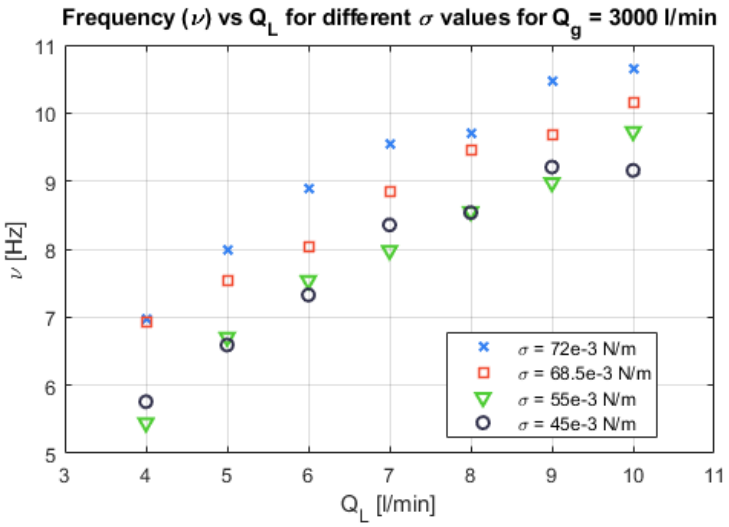


Figure 14. DW frequency $\nu_{DW}$ (Hz) for different values $Q_l$ in litters/min and $Q_g = 3000\,\frac{l}{m}$ and different surface tensions in N/m (series1, 72 $10^{-3}$, series 2, 68.5 $10^{-3}$, series 3, 55. $10^{-3}$, series 4, 45. $10^{-3}$)

## 4. Discussion of results and correlations

When performing the analysis of the results and the development of the new correlations for the different magnitudes, it is necessary to consider which non-dimensional numbers must be included in the correlations for the main magnitudes. In particular, non-dimensional numbers have been used to characterize all annular flow magnitudes, as

mean film thickness, unperturbed film thickness, amplitude and frequency of the disturbance waves. It is well known (Cuadros et al. 2019), that the Reynolds numbers of the gas $Re_g$ and liquid $Re_l$ phases play a fundamental role in the characterization of these magnitudes. However, these Reynolds numbers are normally expressed in experimental applications in terms of the superficial velocities $j_g$ and $j_l$ as follows:

$$Re_g = \frac{\rho_g j_g D}{\mu_g} \tag{11}$$

$$Re_l = \frac{\rho_l j_l D}{\mu_l} = \frac{4\Gamma}{\mu_l} \tag{12}$$

Where Γ is the liquid mass flow rate of the film flow per unit of circumferential length. However, this last assertion is true when there is not entrainment of the film by the gas flow, which verifies only for low gas superficial velocities, but not for high superficial velocities, condition that usually take place in vertical annular co-current flow. In this case, to characterize properly the flow characteristics of the film, we must consider the entrainment fraction, and to take into account a corrected liquid film Reynolds number, which is given by:

$$Re_{film,l} = \frac{\rho_l J_l (1-E) D}{\mu_l} = \frac{4\Gamma(1-\mathrm{E})}{\mu_l} \tag{13}$$

Being E the entrainment fraction, which can be measured or obtained from correlations. However, it is common practice to express the correlations in terms of expression (12).

In annular two-phase flows with a gaseous core that exerts a shear stress on the gas-liquid interface, as mentioned in the introduction, three types of waves are shown: disturbance, ripples and ephemeral. Obviously, the shear stress depends on the relative velocity of both phases. Because of the liquid velocity is small compared with the gas velocity, then the shear stress depends in a first approximation on the gas velocity, and the friction factor which is a function of the gas Reynolds number. Oron et al. (1997) studied the Navier-Stokes equations in film flow and the boundary condition which must be satisfied at the gas-liquid interface. The balance of forces at the liquid-gas interface lead to the following equation for the stress force $\vec{t}$ at the interface:

$$\vec{t} = -p\vec{n} + \overleftrightarrow{\tau_l}.\vec{n} = -\sigma\,\kappa\,\vec{n} + \vec{f}_{ex} \tag{14}$$

Where $\kappa$ is the film curvature, $\vec{n}$ is the normal vector to the interface, and $\vec{f}_{ex}$ denotes the interfacial forces due to the gas, p is the pressure, and $\overleftrightarrow{\tau_l}$ is the shear stress tensor of the liquid. The first term of the right-hand side depends on the surface tension and the film curvature. This term, when nondimensionalized, will produce the dependence of the Navier-Stokes equations with the Kapitza number.

The surface wave characteristics depend on liquid surface tension and viscosity, and in addition, on the gas and liquid velocities, these last two magnitudes are incorporated into the gas and liquid Reynolds numbers. To take into account the effect of the surface tension $\sigma$, we can use two non-dimensional numbers the Weber and Kapitza numbers. Weber number is denoted by We, which is the ratio of the inertial to the surface tension forces. While the Kapitza number, denoted by Ka, and which can be defined in two different ways, the first one defines this non-dimensional number as the square of the ratio of the

capillarity length, $l_{cap}$, and the characteristic length of the fluid, $l_v$, which has advantage to be independent of the flow characteristics, so we have:

$$Ka = \left(\frac{l_{cap}}{l_v}\right)^2 = \frac{\sigma}{\rho_l g^{1/3} \nu_l^{4/3}} \tag{15}$$

Where the characteristic lengths $l_{cap}$ and $l_v$ are defined by means of the expressions:

$$l_{cap} = \sqrt{\frac{\sigma}{\rho_l g}} \quad , l_v = \left(\frac{\nu^2}{g}\right)^{1/3} \tag{16}$$

The Kapitza number can be also defined as the ratio of the surface to gravitational forces, choosing the characteristic length as $l_v$, it is obtained again equation (15):

$$Ka = \frac{(\sigma/l_v)}{(\varrho_l g l_v)} = \frac{\sigma}{\rho_l g^{1/3} \nu_l^{4/3}} \tag{17}$$

Because of the considerations of the previous discussion, we have performed the fitting, to obtain the correlations for the physical magnitudes, in terms of $Re_g, Re_l$ and $Ka$ and also in terms of $Re_g, Re_l$ and $We$, obtaining slightly better results with $Re_g, Re_l$ and $Ka$.

4.1 Mean film thickness

The experimental data for the non-dimensional mean film thickness, $\bar{\delta}_m/D$, were correlated in terms of $Re_g$ for the gas superficial velocity given by expression (11), the Reynolds of the liquid $Re_l$ given by expression (12), and the Kapitza number Ka, defined by equation (15). A total number of 196 experimental data points were used to obtain this correlation, which is given by the following expression:

$$\frac{\bar{\delta}_m}{D} = 2.35\, Re_l^{0.414}\, Re_g^{-1.415} Ka^{0.781} \tag{18}$$

The coefficient of determination obtained for this correlation is $R^2 = 0.98$, and the root mean square error for $\bar{\delta}_m$ is $RMSE\ (\bar{\delta}_m) = 0.0299\ mm$. Figure 15 displays the measured values versus the fit results for the average mean film thickness. It is clear, from this correlation, that the mean film thickness diminishes with the gas Reynolds number, and increases with the Kapitza number and $Re_l$. The advantage of this correlation, equation (18), is that provides the mean film thickness for different values of the Kapitza number, i.e., when the surface tension of the liquid changes.

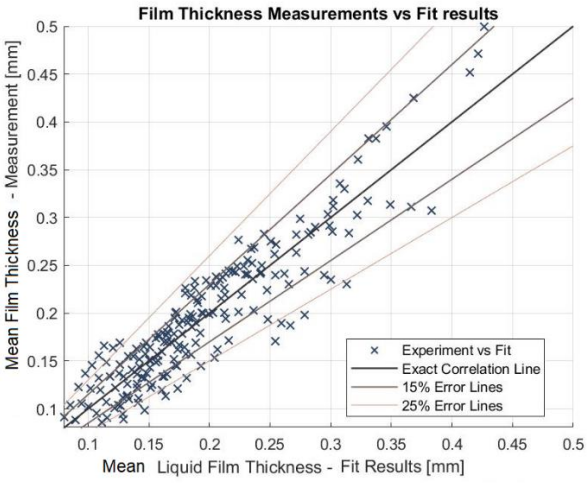


Figure 15. Experimental data versus correlation predictions for the mean film thickness.

A preliminary analysis of the correlation given by eq (18) and the experimental data of table (7) shows that the mean film thickness increases with the liquid Reynolds and the Kapitza number and diminishes with the gas Reynolds number. This reduction with the gas Reynolds number is produced by two effects, the first one is that the shear stress produced by the gas cut the peaks of the disturbance waves and drag drops, while the second one is that the shear stress exerted by the gas on the interface reduces the mean thickness of the film.

4.2 Height and Amplitude of the disturbance waves

The average height of the DWs, $\bar{\delta}_{DW}$, and their average amplitudes, $A_{DW}$, see figure 8, are key factor to characterize the DW. Obviously, the gas velocity has a great effect on these two magnitudes because both are affected by the liquid entrainment produced on the crest of the DW. In earlier studies, Woodmansee and Harrantty (1969) showed evidences that the production of drops from the film in the channel walls took place at the crests of the DWs. Later, Azzopardi (2006) found more evidences of this effect, which obviously affects the height and the amplitude of the DWs. For this reason, it is expected that the height of these waves will reduce when increasing the gas velocity. Also, from physical considerations related to the curvature terms that appears in the Navier-Stokes equations for film flow (Oron et al. 1997), it is expected that the height of these waves will increases with the Kapitza number. Then, from the data of the experiments performed at the VAFF facility with different surface tensions, we have found that the height of the DW can be correlated by the expression:

$$\frac{\delta_{DW}}{D} = 0.554\ 10^{-3} Re_l^{0.061} Re_g^{-0.57} Ka^{1.12} \qquad (19)$$

The coefficient of determination was $R^2 = 0.9757$, and the root mean square error for $\delta_{DW}$ was $RMSE\ (\bar{\delta}_{DW}) = 0.0928\ mm$. Figure (16-a) displays the experimental value versus the obtained from the correlation (19) for the average total height of the DW, $\delta_{DW}$.

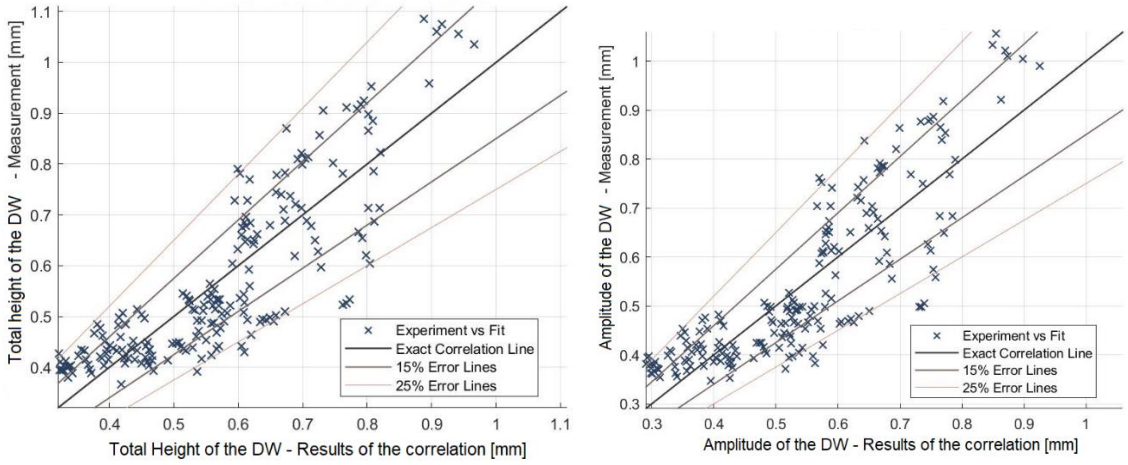


(a) (b)

Figure 16. Experimental data versus correlation predictions for the mean height of the DW (a) and the amplitude of the DW (b).

In addition, from the experimental data for the amplitude $A_{DW}$ of the DW, obtained in the VAFF facility for different superficial tensions, we have correlated the non-dimensional amplitude of the DW, i.e., $A_{DW}/D$, in terms of $Re_l$, $Re_g$, and Ka:

$$\frac{A_{DW}}{D} = 0.245\ 10^{-3}\ Re_l^{0.0479} Re_g^{-0.551} Ka^{1.203} \tag{20}$$

The coefficient of determination was $R^2 = 0.9737$ and the root mean square error for $A_{DW}$ was $RMSE\ (A_{DW}) = 0.0917\ mm$.

It is observed in both correlations that the height and the amplitude of the DWs diminish with the gas Reynolds number, $Re_g$, and increases with the Kapitza number, Ka, and are practically independent of liquid Reynolds number, $Re_l$.

4.3 Frequency of the disturbance waves

The DW frequency is defined as the number of large peaks associated to DW per time unit and it is obtained counting the number of peaks of the disturbance waves in a given sampling interval, and dividing by the sampling time. To non-dimensionalize the DW frequency, we have used the Strouhal number, which can be expressed in terms of the gas superficial velocity as follows (Cuadros et al. 2019):

$$St_g = \frac{\bar{v}_{DW} D}{j_g} \tag{21}$$

Performing the fit of the Strouhal number experimental data in terms of $Re_l$, $Re_g$ and the Ka numbers, the following correlation is obtained:

$$St_g = 0.262\ Re_l^{0.266} Re_g^{-0.79} Ka^{0.46} \tag{22}$$

The coefficient of determination of this correlation was $R^2 = 0.9845$, and the root mean square error was $RMSE\ (St_g) = 0.0016$. Figure 17 displays the experimental versus the calculated gas Strouhal number using equation (22).

In addition, another fit was performed directly with the DW frequency in terms of the same non-dimensional numbers, as carried out in equation (20), the correlation obtained in this case was:

$$\nu_{DW}(Hz) = 0.003468\, Re_l^{0.347} Re_g^{0.197} Ka^{0.343} \qquad (23)$$

The coefficient of determination for this last equation was $R^2 = 0.9863$, and the root mean square error was 1.0 Hz.

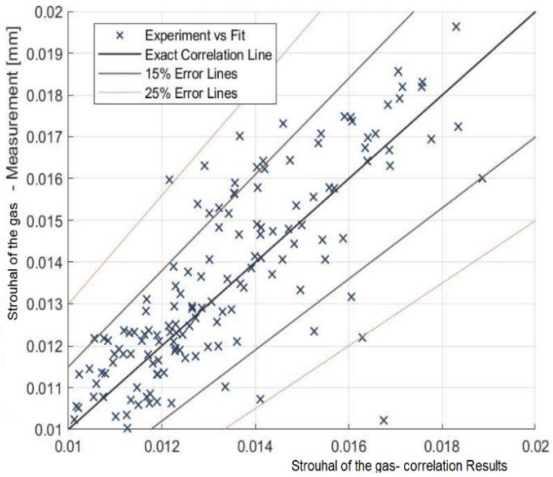


Figure 17. Experimental data versus correlation predictions for the gas Strouhal number

4.4. Velocity of the disturbance waves

Belt et al. (2010) have measured the velocity of the disturbance waves in a vertical pipe of inner diameter of 0.05 m with an annular flow configuration, with water and air concurrent flows at ambient conditions, i.e., injecting dry air and water at the bottom of the test pipe. The film thickness and other parameters, as the velocity of the disturbance waves, were measured for different gas and liquid superficial velocities. Because some of the boundary conditions for the tests with water were close to our boundary conditions, we can perform a cross-comparison for some particular cases of the mean interfacial velocity of the disturbance waves, $C_{DW}$. They found that for a fixed gas superficial velocity, $j_g$, the velocity of the DW increases with the liquid superficial velocity, $j_l$, until it attains an asymptotic value for superficial velocities of the liquid larger than 0.08 m/s. Also, they found that for fixed liquid superficial velocity, the DW velocity $C_{DW}$ increases with the gas superficial velocity.

Marmottant and Villermaux (2004) deduced the formula for the waves velocity in coaxial jets, also Belt et al. (2010) used Marmottand and Villermaux formula. Berna et al (2014) developed a new expression in terms of dimensionless numbers given by:

$$C_{DW} = \frac{\sqrt{\rho_g} j_g + \sqrt{\rho_l} j_l}{\sqrt{\rho_g} + \sqrt{\rho_l}} \cdot 50 \cdot {Re_g}^{-0.38} \cdot {Re_l}^{0.16} \cdot {C_W}^{-0.13} \qquad (24)$$

Where $C_W$ corresponds to a factor related with the surface tension, which is defined as follows:

$$C_W = 0.028 \cdot {N_\mu}^{-4/5} \;\; ; \;\; N_\mu = \frac{\mu_l}{\sqrt{\rho_l \cdot \sigma \sqrt{\frac{\sigma}{g\Delta\rho}}}} \qquad (25)$$

The expression of $C_W$ could be applied when the viscosity number $N_\mu$ is less or equal to $1/15$, otherwise, $C_W$ is equal to 0.25.

Comparison of the results with the experimental measurements of Belt et al. (2010) shows a good agreement. For low liquid and gas superficial velocities, closer predictions have been reached, as for high liquid and gas superficial velocities. However, for low liquid – high gas and high liquid – low gas velocities the differences are a little bit higher.

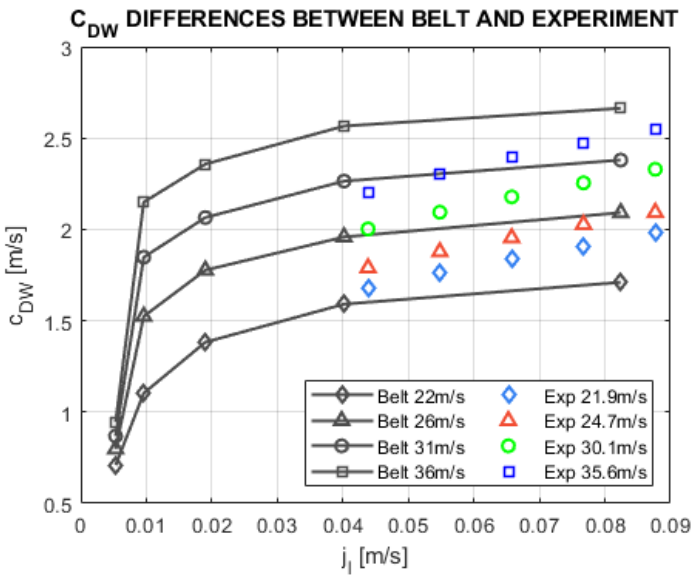


Figure 18. Average velocity of the DW, in the laboratory reference system versus the liquid superficial velocity for different gas superficial velocities obtained by Belt et al., and comparison with the results of this paper using equation (24).

4.5 Average thickness of the unperturbed base film plus RW, amplitude of the ripple waves and amplitude of the unperturbed film thickness

The main magnitudes that characterize the small incoherent waves, denoted as RW, are the average thickness of the unperturbed base film plus the amplitude of the RW, denoted by $\bar{\delta}_{RW}$, and the amplitude of the RW, $A_{RW}$. Table 5 displays these amplitude values for several representative cases, and as shown in the table, this amplitude is influenced by the surface tension value. It is observed in table 3 that, in general, the amplitude $A_{RW}$ of the RW diminishes when the surface tension diminishes, for all the gas superficial velocities that are below or equal to $j_g = 27.4\, m/s$ ($Q_g = 2500\ lit/m$), while for all the liquid superficial velocity values above this $j_g$ value there is not a clear tendency. Also, it is observed that $A_{RW}$ increase when $j_l$ rises for all the values of $j_g$ and more clearly that $A_{RW}$ diminishes when $j_g$ increases.

To quantify this behavior, we have performed a fit of $\frac{A_{RW}}{D}$ in terms of $Re_l$, $Re_g$, and $Ka$, using the non-linear fitting routine of MATLAB. The correlation obtained for $\frac{A_{RW}}{D}$ using the 196 available experimental points to perform the fit is:

$$\frac{A_{RW}}{D} = 0.084\, Re_l^{0.249} Re_g^{-0.896} Ka^{0.553} \tag{26}$$

The coefficient of determination was $R^2$=0.98, and the root mean square error RMSE=0.015 mm. Finally, figure 19 displays the experimental versus the calculated $A_{RW}$ values.

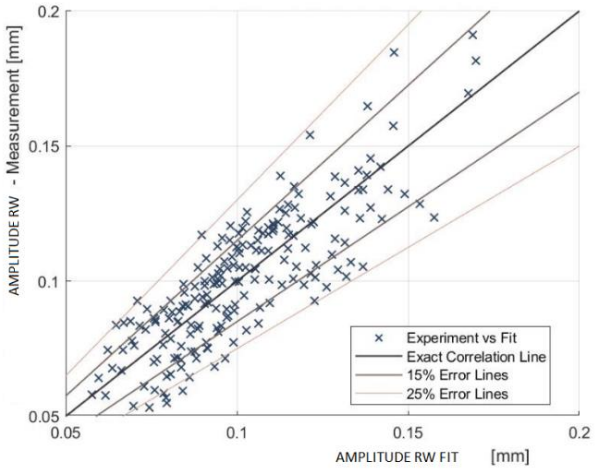


Figure 19. Experimental data versus correlation predictions for the amplitude of the RW.

In addition, the correlation obtained for $\bar{\delta}_{RW}$ is given by the expression:

$$\frac{\bar{\delta}_{RW}}{D} = 0.3175\, Re_l^{0.27} Re_g^{-0.895} Ka^{0.4} \tag{27}$$

With a coefficient of determination $R^2 = 0.982$, and RMSE=0.018 mm for $\bar{\delta}_{RW}$.

Concerning the base film thickness that remains unperturbed by the disturbance waves (DW) or he ripples waves (RW), and that it is denoted by $\bar{\delta}_{bun}$; we have correlated this non-dimensionalized film thickness with $Re_l$, $Re_g$ and $Ka$, as previously, obtaining the result:

$$\frac{\bar{\delta}_{bun}}{D} = 1.48\, Re_l^{0.347} Re_g^{-0.889} Ka^{-0.054} \tag{28}$$

The coefficient of determination was $R^2 = 0.977$ and RMSE=0.005 mm for $\bar{\delta}_{bun}$. It is observed that the base unperturbed film thickness increases slowly with the liquid Reynolds and diminishes with the gas Reynolds almost linearly. This base unperturbed film thickness is not influenced by the Kapitza number, this means that is practically insensitive to the changes in the surface tension.

4.6 Comparison with the correlations of other authors

In this subsection, we compare the results of the correlations obtained in the previous sections for the different physical magnitudes with the results of the correlations of other authors and the experimental data obtained in this paper. The first physical magnitude to

be compared is the mean film thickness $\bar{\delta}_m$, that is compared with the correlations by Pan et al. (2015) and the Berna et al. (2014), which are given respectively by the following expressions:

$$\frac{\bar{\delta}_m}{D} = 2.03\, Re_{lf}^{0.15} Re_g^{-0.6}\,, \tag{29}$$

$$\frac{\bar{\delta}_m}{D} = 7.165\, Re_l^{0.48} Re_g^{-1.07} \left(\frac{Fr_g}{Fr_l}\right)^{0.24}\,, \tag{30}$$

where the film Reynolds number in equation (26) is given by $Re_{lf} = (1-E)Re_l$, being E the entrainment fraction, and $Fr_g$ and $Fr_l$, are the gas and liquid Froude numbers respectively, defined in terms of the superficial velocities. Figure 20 gives the results obtained for the mean film thickness versus the gas Reynolds number at different boundary conditions, i.e., different $Re_l$ with $\sigma = 72.10^{-3}$N/m. It is observed that $\bar{\delta}_m$ diminishes when the gas Reynolds number increases. Also, one notices that Berna et al. (2014) correlation is lower than the experimental data for $Re_g < 75000$. When the surface tension decreases to $\sigma = 45.10^{-3}$N/m, the average mean film thickness decreases, as observed in figure (21). However, this behavior is well predicted by the correlation obtained in this paper but Pan et al. correlation is above the experimental results for all the cases, and Berna et al. correlations (2014) over predicts a little bit some of the experimental data.

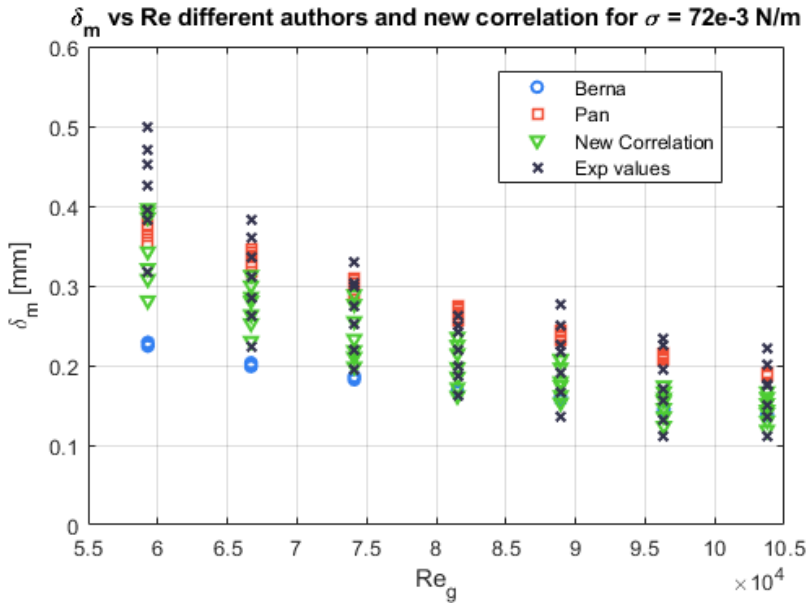


Figure 20. Mean film thickness versus $Re_g$ for the different run cases performed at different $Re_l$, and $\sigma = 72.10^{-3} N/m$. The circles are the results obtained with Berna et al. (2014) correlation, the squares denote the results obtained with Pan et al. (2015) correlation, the triangles denote the results obtained with the correlation given by eq. (16) of this paper, and the Saint Andrew crosses are the experimental results of this paper.

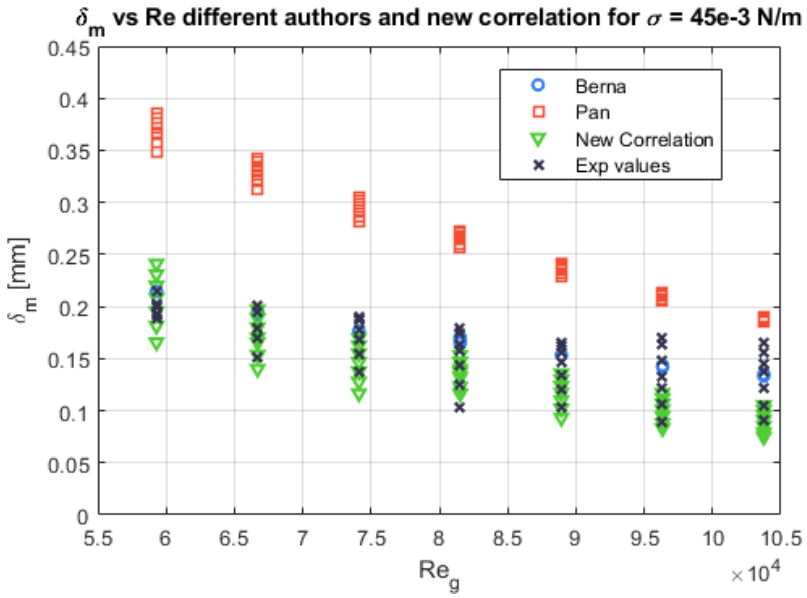


Figure 21. Mean film thickness versus $Re_g$ for the different run cases performed at different $Re_l$, and $\sigma = 45.10^{-3} N/m$. The circles are the results obtained with Berna et al. (2014) correlation, the squares denote the results obtained with Pan et al. (2015) correlation, the triangles denote the results obtained with the correlation given by eq. (16) of this paper, and the Saint Andrew crosses are the experimental results of this paper.

Another important physical parameter to characterize the film thickness is the amplitude of the disturbance waves, $A_{DW}$, this amplitude can be affected by two causes. The first one is that the gas velocity entrain droplets from the peaks of the disturbance waves, reducing their height. While the second one is that the amplitude of this waves depends on the surface tension and increases with it as proved by Chandrasekar (1981), therefore it is expected that $A_{DW}$ will reduce when diminishing $\sigma$. The height of the disturbance waves will depend in general of $Re_g$, $Re_l$ and the $Ka$. The results for $A_{DW}$ will be projected on the planes $(A_{DW}, Re_g)$ and $(A_{DW}, Re_l)$ for fixed values of $\sigma$. In addition, we will compare the results obtained by Han et al. correlation (2006) for $A_{DW}$ with the results of Chandrasekar formula (1981) for the amplitudes of the waves of the Helmholtz- Kelvin instability, which are respectively given by:

$$\frac{A_{DW}}{D} = 4.10^3 / Re_g^{1.12} \tag{31}$$

$$A_{DW} = 3\pi \frac{\sigma_l (1+(\rho_g/\rho_l))}{\rho_g (u_g - u_l)^2} \tag{30}$$

Where $u_l$ is the mean velocity in the film, and $\sigma_l$ the liquid surface tension.

Figure 22 displays the results obtained for $A_{DW}$ with Han et al. (2006) and Chandrasekar expressions given by equations (28) and (29), respectively. Also this figure displays the experimental results and the results obtained with equation (18) of this paper. Obviously Chandrasekar equation for the amplitude over predict the results because does not consider the effect of the drop entrainment performed by the gas and that reduces the effective height of the DW peaks.

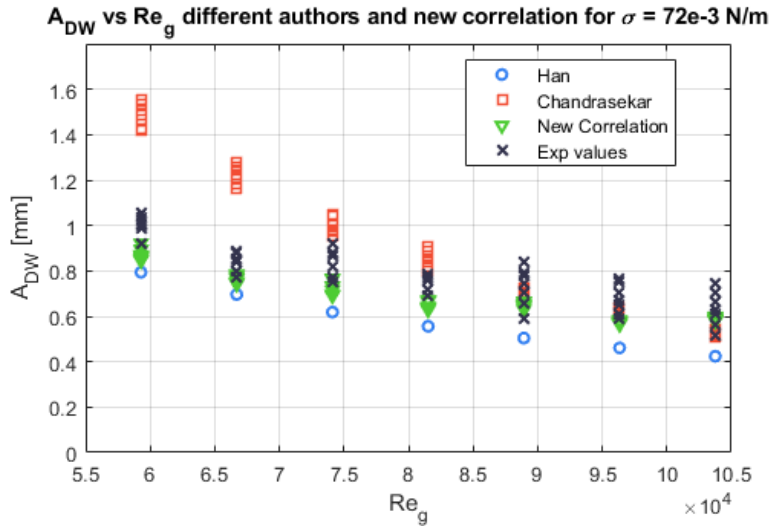


Figure 22. Mean amplitude of the DW versus $Re_g$ for the different runs performed at different $Re_l$, and $\sigma = 72.10^{-3} N/m$. The circles are the results obtained with Han et al. (2006) correlation, the squares denote the results obtained with Chandrasekar et al. (1981) correlation, the triangles denote the results obtained with the correlation given by eq. (18) of this paper, and the Saint Andrew crosses are the experimental results of this paper.

The figure 23 displays $A_{DW}$ versus the $Re_g$ number for the different values of $Re_l$. Obviously, Chandrasekar expression and Han correlation over predict the experimental values except at very high gas Reynolds numbers, where all the expressions give approximately values that are close. The reason for this over prediction is that Han expression is calculated for pure water that has higher Kapitza number and, therefore, the amplitude of the peaks is higher. In addition, Chandrasekar expression also over predicts the DW amplitude because does not considers the entrainment of drops from the peaks of the DW. Also, diminishing the surface tension reduces the cohesion forces in the water and makes easier the entrainment, reducing more the height of the peaks.

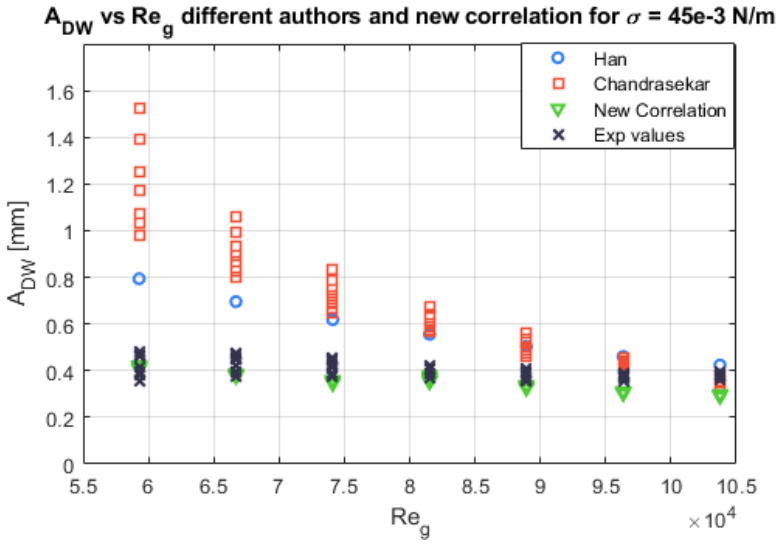


Figure 23. Mean amplitude of the DW versus $Re_g$ for the different runs performed at different $Re_l$, and $\sigma = 45.10^{-3} N/m$. The circles are the results obtained with Han et

al.'s (2006) correlation, the squares denote the results obtained with Chandrasekar et al.'s (1981) correlation, the triangles denote the results obtained with the correlation given by eq. (18) of this paper, and the Saint Andrew crosses are the experimental results of this paper.

Also, it is interesting to display $A_{DW}$ versus $Re_l$, to see the influence of liquid Reynolds number on the amplitude of the disturbance waves. Figure 24 displays $A_{DW}$ versus $Re_l$ for all the experiments performed with different $Re_g$, and water with a surface tension $\sigma = 72.10^{-3}$N/m. The variations of $A_{DW}$ with $Re_l$ are very small, the observed variations in $A_{DW}$ , displayed on figure (22), are mainly produced by the changes in $Re_g$, this fact is confirmed by the exponent of $Re_l$ in equation (18) that is equal to 0.0479. Chandrasekar's expression, eq. (29), clearly over predicts $A_{Dw}$ as displayed in figure 22, while Han et al.'s correlation predicts a range of amplitudes between 0.4 mm and 0.8 mm, which is close to the range predicted by the correlation (18) of this paper, that gives values between 0.5 mm and 0.9 mm. When the surface tension diminish to $\sigma = 45.10^{-3}N/m$, it is observed that $A_{DW}$ practically does not change with $Re_l$, and the range of variation for different $Re_g$ reduces to small variations between 0.35 mm and 0.48 mm for the lower $Re_l = 2064$ and even smaller range, between 0.36 mm and 38 mm, for $Re_l = 5100$.

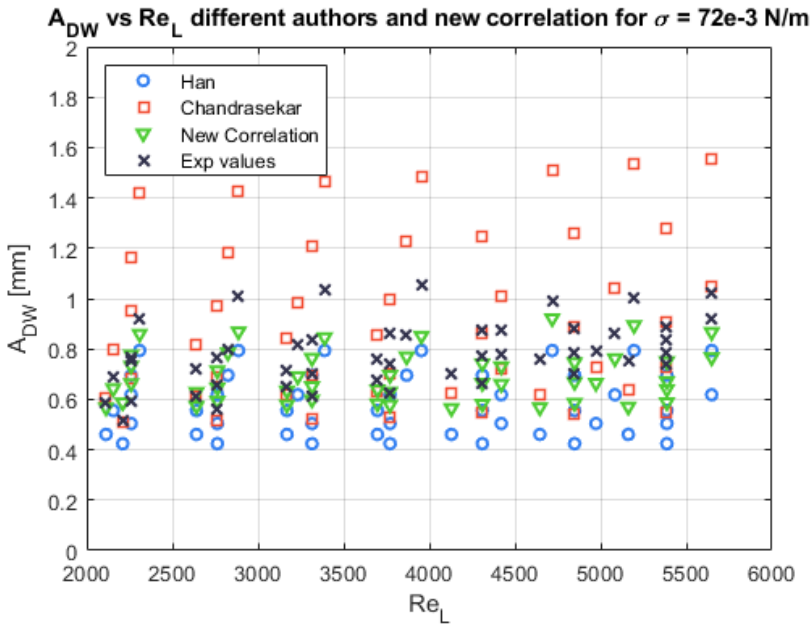


Figure 24. Mean amplitude of the DW versus $Re_l$ for the different runs performed at different $Re_g$, and $\sigma = 72.10^{-3}N/m$. The circles are the results obtained with Han et al.'s (2006) correlation, the squares denote the results obtained with Chandrasekar et al.'s (1981) correlation, the triangles denote the results obtained with the correlation given by eq. (18) of this paper, and the Saint Andrew crosses are the experimental results of this paper.

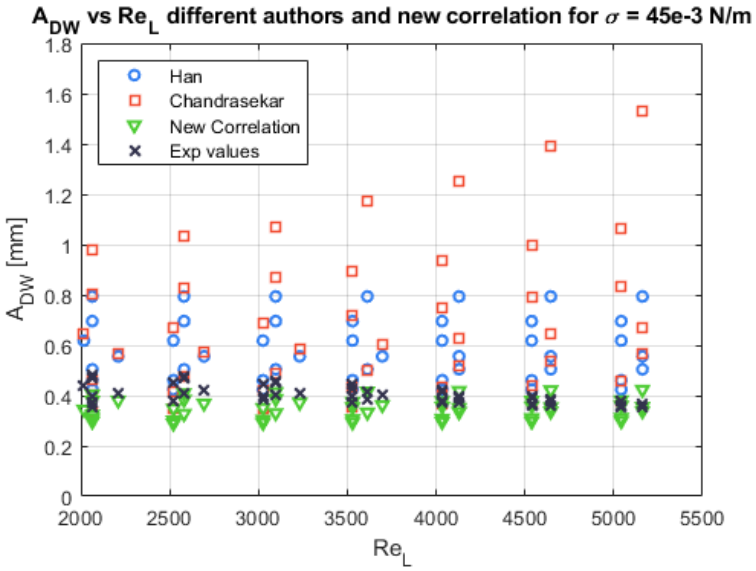


Figure 25. Mean amplitude of the DW versus $Re_l$ for the different runs performed at different $Re_g$, and $\sigma = 45.10^{-3} N/m$. The circles are the results obtained with Han et al.'s (2006) correlation, the squares denote the results obtained with Chandrasekar et al.'s (1981) expression, the triangles denote the results obtained with the correlation given by eq. (18) of this paper, and the Saint Andrew crosses are the experimental results of this paper.

The last comparison performed was with the results obtained by Alamu and Azzopardi (2011), for the Strouhal number of the DW, the experimental results of this paper, and the two correlations obtained in this paper for the Strouhal number:

$$St_l = 0.429\, X^{-0.908} \tag{32}$$

Being X the Lockhart–Martinelli parameter defined by the expression:

$$X = \sqrt{\frac{\rho_l j_l^2}{\rho_g j_g^2}} \tag{33}$$

It is observed that the DW frequency, $\nu_{DW}$, versus $Re_l$ obtained using the correlations of this paper, given by equations (20) and (21), is within the limits of the frequency obtained by Alamu and Azzopardi (2011), for the lower $Re_l$ and in the upper part for higher $Re_l$ values, for the different $Re_g$ values, as displayed in figure 23, for the water and increases with the $Re_l$. When the surface tension diminishes from $72.10^{-3}$ N/m to $45.10^{-3}$ N/m, by adding small quantities of 1-butanol, the overall behavior is that the DW frequency, $\nu_{DW}$, versus $Re_l$ still increases, as displayed in figure 25, but the values are smaller. Both correlations, (22) and (23), show that the frequency and the Strouhal number increase with the Kapitza number, so that for the same gas and liquid Reynolds numbers $\nu_{DW}$ increases with the surface tension because the density and the kinematic viscosity are very little affected by the small amounts of 1-butanol added. Concerning the change of $\nu_{DW}$ with $Re_g$, it is observed that $\nu_{DW}$ increases with $Re_g$, for Alamu and Azzopardi correlation, as displayed in figure 24 and 26. An increment of $\nu_{DW}$ with $Re_g$, it is also observed in correlations (22) and (23), but these increments are smaller than the obtained by Alamu and Azzopardi. The frequency changes proportionally to $j_g^{0.2}$, as deduced from

equations (22) and (22), this small exponent is probably caused by the surface tension effects.

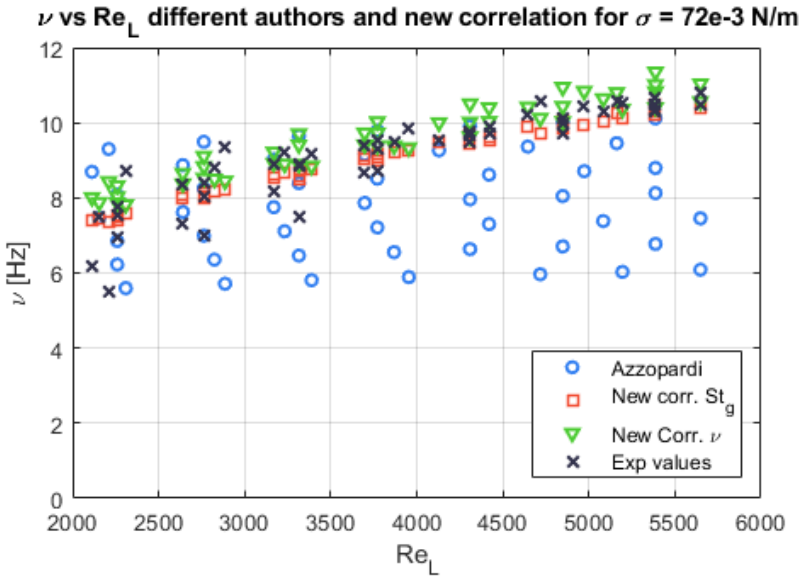


Figure 26. DW frequency values versus $Re_l$ for $\sigma = 72.10^{-3} N/m$ and different $Re_g$, obtained with Azzopardi correlation (2011) (circles), the correlation of this paper, equation (22) (squares), the second correlation of this paper for the frequency, equation (23) (triangles) and the experimental data (Saint Andrew crosses).

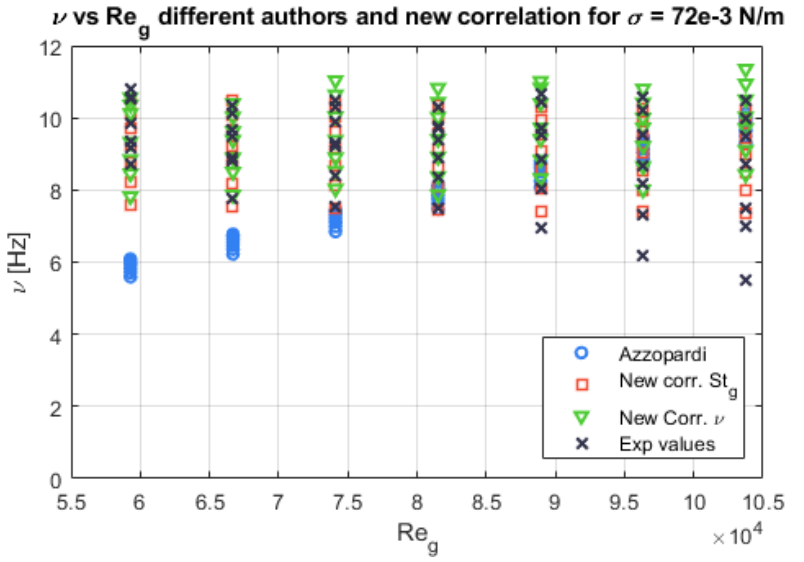


Figure 27. DW frequency values versus $Re_g$ for $\sigma = 72.0\ 10^{-3} N/m$ and different $Re_l$ values obtained with Azzopardi's correlation (2011) (circles), the correlation of this paper, equation (22) (squares), the second correlation of this paper for the frequency, equation (23) (triangles) and the experimental data (Saint Andrew crosses).

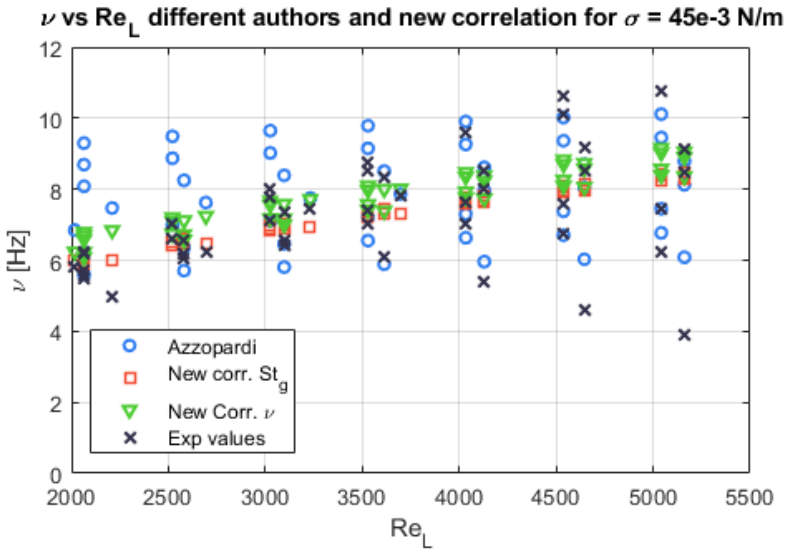


Figure 28. DW frequency versus $Re_l$ for $\sigma = 45.10^{-3}\frac{N}{m}$ and different $Re_g$ values obtained with Alamu and Azzopardi's correlation (2011) (circles), the correlation of this paper, equation (22) (squares), second correlation of this paper, equation (23) (triangles) and the experimental data (Saint Andrew crosses).

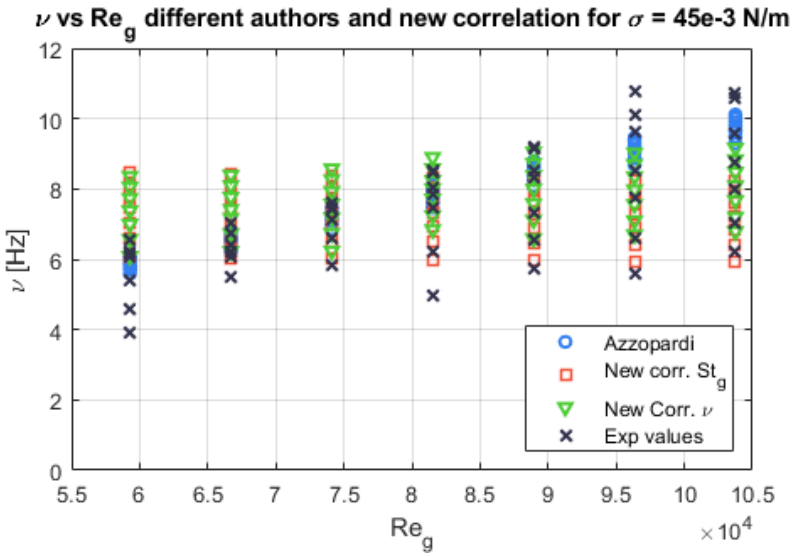


Figure 29. DW frequency versus $Re_g$ for $\sigma = 45.10^{-3}\ N/m$ and different $Re_l$ values obtained with Alamu and Azzopardi's correlation (2011) (circles), the correlation of this paper, equation (22) (squares), second correlation of this paper, equation (23) (triangles) and the experimental data (Saint Andrew crosses).

## 5. Conclusions

The study of the variations produced in the physical magnitudes that characterize the gas-liquid interface when changing the surface tension, and the gas and liquid superficial velocities in annular vertical concurrent two-phase flow has been the main goal of this paper. Many experiments have been performed in the past (Alamu and Azzopardi 2011, Belt et al. 2010, Alekseenko et al. 2010) with pure water, but very few changing the

surface tension of the water and maintaining the value of the viscosity. This has been possible adding small amounts of 1-butanol to the water, which has the property of changing the surface tension of the water, $\sigma$, while maintaining practically constant the dynamic viscosity, $\mu$. The range of surface tensions selected was from $0.072\ N/m$ equal to the surface tension of the water at 25 ºC and $p = 1$ atm to $0.045\ N/m$ that is below the surface tension at boiling conditions and $p = 1\ atm$. We performed experiments at water surface tension of $\sigma = 0.072\frac{N}{m}$, $0.0685\frac{N}{m}$ , $0.055\frac{N}{m}$ and $0.045\ N/m$ with a broad range of superficial velocities of the gas and liquid phases, as displayed at table 2, which covers a broad range of applications for the correlations developed in this paper.

In general, it is observed that the amplitude of the DW and the RW diminishes when increasing the superficial velocity of the gas for all the surface tension values as showed in tables (8) and (5). This effect is caused by two mechanisms, the first one is that increasing the gas velocity increases the shear stress exerted by the gas on the peaks of the DW and this effect drags small drops from the crest of these peaks. The second one is that reducing the surface tension by adding 1-butanol to the water, it reduces the intermolecular cohesion forces and makes easier that the gas drags small drops from the peaks of the waves reducing the DW amplitude when the surface tension diminishes as observed in table 8. This same effect is also observed in the dependence of $A_{DW,}$ found in this paper, with the Kapitza number given by equation (20), which is proportional to $Ka^{1.12}$. In addition, it is noticed that the dependence of $A_{DW}$ with $Re_g$ becomes smaller at lower surface tension values, as observed comparing figures 22 and 23.

The unperturbed base film thickness, $\delta_{bun}$, diminishes when $Re_g$ increases, probably due to the shear stress exerted on the interphase by the gas moving at higher velocity, being this effect observed for all the surface tension values, as displayed in table 6. Also diminishing with $Re_g$ the amplitude of the ripple waves. In addition, $A_{RW}$ diminishes when the surface tension becomes smaller.

The DW frequency, $\nu_{DW}$, increases with $Re_l$ for all the surface tension values, as it is observed comparing figures 26 and 28, and also in the correlation given by equation (23). However the dependence of $\nu_{DW}$ with $Re_g$, given by expression 23, is smaller than the one found by other authors, as Alamu and Azzopardi for water (2011), which depends on $Re_g^{0.902}$, while for the expression found in this paper $\nu_{DW} \propto Re_g^{0.2}$. The explanation of this fact could be that increasing the gas velocity increases the shear stress acting on the interphase and this perturbation increases the number of DW per second. But, at the same time, when the surface tension diminishes maintaining the viscosity practically constant the height of the peaks diminishes, because the Kapitza number that governs the term that depends on the interphase curvature, with a decreasing tendency. In addition, the cohesion forces in the water diminish, so drops are easily dragged from the crest of the peaks and, in general, the height of all the peaks become smaller when reducing the surface tension. So it is expected a reduction of the exponent of the dependence of the DW frequency with $Re_g$ at lower $Ka$ numbers, as happens according to the experimental results, figures 26 and 28 and equation (23).

**Acknowledgements**

This work was supported by the project EXMOTRANSIN ENE2016-79489-C2-1-P of the Spain National Research I+D Plan.

**References**

Alamu, M.B., Azzopardi, B.J., 2011. Wave and drop periodicity in transient annular flow, Nuclear Engineering and Design 241 (2011) 5079–5092.

Alamu, M.B., Azzopardi, B.J., 2011. Simultaneous investigation of entrained liquid fraction, liquid film thickness and pressure drop in vertical annular flow. J. Energy Resource. Technol. Trans. ASME 133 (023103), 1–10, doi:10.1115/1.4004265.

Azzopardi, B.J., 1997. Drops in Annular two-phase flow, Int. J. Multiphase Flow Vol. 23, Suppl., pp. 1-53.

Azzopardi, B. J. and Whalley, P. B., 1980. Artificial waves in annular two-phase flow. ASME Winter Annual Meeting, Chicago, Published in Basic Mechanisms in Two-Phase Flow and Heat-Transfer, pp. 1-8.

Alekseenko, S.V., Cherdantsev, A.V., Heinz, O.M, Kharlamov, S.M., Markovich, D.M., Analysis of spatial and temporal evolution of disturbance waves and ripples in annular gas–liquid flow, International Journal of Multiphase Flow Vol 67 (2014) pp 122–134.

Belt, R.J., Van't Westende, Prasser, H.M., Portela, L.M., Time and spatially resolved measurements of interfacial waves in annular flow, International Journal of Multiphase Flow, vol 36, pp 570-587 (2010).

Bevington, P.R., Robinson, D.K., Data Reduction and Error Analysis in the Physical Sciences, Third Edition, edited by Mac Graw Hill (2003).

Chandrasekhar, S., 1981. Hydrodynamic and Hydromagnetic Stability. Oxford University Press.

Chu, K.J., Dukler, A.E., 1974. Statistical characteristics of thin, wavy films: Part II. Studies of the substrate and its wave structure. AIChE J. 20, 695–706.

Coney, M.E., 2001, The theory and application of conductance probes for the measurement of liquid film thickness in two-phase flow, 1973 J. Phys. E: Sci. Instruments. 6 pp 903-910.

Cuadros, J.L., Rivera, Y., Berna, C., Escrivá, A., Muñoz-Cobo, J.L., Monrós-Andreu, G., Chiva, S., 2019, Characterization of the gas-liquid interfacial waves in vertical upward co-current annular flows, Nuclear Engineering and Design, Vol 346, pp 112–130.

De Jong, P., Gabriel, K.S., 2003. A preliminary study of two-phase annular flow at microgravity: experimental data of film thickness. Int. J. Multiphase Flow 23, pp 1203–1220.

Guiñón, J.L., Ortega, E., García-Antón, J., Pérez-Herranz, V., Moving Average and Savitzki-Golay Smoothing Filters Using Mathcad, Proceedings of the International Conference on Engineering Education, ICEE 2007, Coimbra 3-7 September (2007).

Hall-Taylor, N., Hewitt, G., Lacey, P., 1963. The motion and frequency of large DW in annular two-phase flow of air-water mixtures. Chem. Eng. Sci. 18, 537–552.

Hall-Taylor, N.S., Hewitt, I.J., Ockendon, J.R., Witelski, T.P.,2014. A new model for disturbance waves, *Int. J. Multiphase Flow*, Vol 66, pp 38–45.

Han, H., Zhu, Z., Gabriel, K., 2006. A study on the effect of gas flow rate on the wave characteristics in two-phase gas-liquid annular flow. Nucl. Eng. Des. Vol 236, pp 2580-2588.

Koskie, J. E., I. Mudawar, and W. G. Tiederman. 1989. "Parallel-Wire Probes for Measurement of Thick Liquid Films." *International Journal of Multiphase Flow* 15 (4). Pergamon: 521–30. doi:10.1016/0301-9322(89)90051-7.

Lee, Kyu-Byung, Kim, Jong-Rok, Park, Goon-Cherl and Cho, Hyoung-Kyu, 2016, Feasibility Test of a Liquid Film Thickness Sensor on a Flexible Printed Circuit Board Using a Three-Electrode Conductance Method, Sensors 2017, 17, 42; doi:10.3390/s17010042.

Muñoz-Cobo, J.L., Chiva, S., Méndez, S., Monrós, G., Escrivá, Cuadros. 2017. "Development of Conductivity Sensors for Multi-Phase Flow Local Measurements at the Polytechnic University of Valencia (UPV) and University Jaume I of Castellon (UJI)." Sensors 17 (5). Multidisciplinary Digital Publishing Institute: 1077. doi:10.3390/s17051077.

Oron, A., Davis, S.H., Bankoff, S.G., Long-Scale Evolution of Thin Liquid Films, Reviews of Modern Physics Vol 69, Number 3, 1997.

Pan, L.M., He, H., Hibiki, T., Ishii, M., 2015. Experimental study and modeling of disturbance wave height of vertical annular flow. Int. J. Heat Mass Transf. Vol 89, pp 165–175.

Press, W.H., Teukolsky, S.A., Vetterling, W.T., Flannery, B.P., Numerical Recipes in Fortran, the Art of Scientific Computing, Second Edition, Cambridge University Press (1992)

Rivera, Y., Muñoz-Cobo, J.L., Berna, C., Cuadros, J.L., Escrivá, A., 2019. Experimental study of the interfacial waves produced in upward vertical annular flow when varying the liquid phase surface tension. Published in the proceedings of the conference: computational and experimental methods in multiphase and complex flow X, WIT Transaction on Engineering Science, Vol 123, pp 21-31.

Rodriguez, D.J., 2004. "Characterization of bubble entrainment, interfacial roughness and the sliding bubble mechanism in horizontal annular flow." PhD. Thesis. University of Wisconsin-Madison.

Savitzky, A., Golay, M.J.E. "Smoothing and differentiation of data by simplified least squares procedures" Analytical Chemistry, 36(2), p.1627, (1964).

Zhao, Y., Markides, C., Hewitt, G., 2013. Disturbance wave development in two-phase gas–liquid upwards vertical annular flow. Int. J. Multiphase Flow Vol 55, pp 111–129.